Understanding Perovskite Solar Cells: A Comparative Analysis of Simulation Models and Experimental Outcomes

M.Sc. THESIS

by

Kumar Saumya

(Roll No.- 2103151015)

to

DEPARTMENT OF PHYSICS

INDIAN INSTITUTE OF TECHNOLOGY

INDORE - 453 552, INDIA

June, 2023

Understanding Perovskite Solar Cells: A Comparative Analysis of Simulation Models and Experimental Outcomes

A THESIS

Submitted in partial fulfilment of the

requirements for the award of the degree

of

Master of Science

by

Kumar Saumya

Department OF PHYSICS

INDIAN INSTITUTE OF TECHNOLOGY, INDORE

June, 2023

INDIAN INSTITUTE OF TECHNOLOGY INDORE

CANDIDATE'S DECLARATION

I hereby certify that the work which is being presented in the thesis entitled **Understanding Perovskite Solar Cells: A Comparative Analysis of Simulation Models and Experimental Outcomes** in the partial fulfillment of the requirements for the award of the degree of **Master of Science** and submitted in the **Discipline of Physics, Indian Institute of Technology Indore**, is an authentic record of my own work carried out during the time period from July 2022 to June 2023 under the supervision of **Dr. Onkar S. Game, Assistant Professor, Indian Institute of Technology Indore.**

The matter presented in this thesis has not been submitted by me for the award of any other degree of this or any institute.

Signature of the student with date
07/06/2023
(Kumar Saumya)

This is to certify that the above statement made by the candidate is correct to the best of my knowledge.

Signature of the Supervisor of M.Sc. thesis (with date)
(Dr. Onkar S. Game)

---------- **Kumar Saumya**
has successfully given his M.Sc. Oral Examination held on **06th June 2023**

Signature of Supervisor of M.Sc. thesis
Date:

Convener, DPGC
Date: 8/6/2023

Signature of PSPC Member no. 1
Date: 08/06/2023

Signature of PSPC Member no. 2
Date: 08/06/2023

Dedicated to my loving parents

ACKNOWLEDGEMENT

I would like to begin by expressing my deepest appreciation to my mentor, **Dr. Onkar S. Game**. His consistent guidance and backing were instrumental in the progress and completion of my M.Sc. project. His patience, motivation, and vast experience have been invaluable. He encouraged me to venture beyond my comfort zone of solely conducting experiments and nudged me towards programming and simulations, thereby bolstering my analytical and theoretical thinking capabilities. His advice was pivotal at all stages of my research and while writing this thesis.

I also sincerely appreciate **Prof. Satish B. Ogale** from the Department of Physics at IISER Pune and Dr. Rupesh S. Devan from the MEMS Department at IIT Indore for granting me access to their labs for experiments. I am likewise grateful to Prof. K.C James Raju from the University of Hyderabad and Prof. Manish Kumar Kashyap from Jawaharlal Neharu University for entrusting me with summer and winter projects under their respective guidance, validating my research capabilities.

Besides my advisor, I wish to convey my sincere gratitude to Prof. Preeti A. Bhobe and Dr. Alestin Mawrie, my PSPC committee members, whose support and motivation have been invaluable.I am deeply thankful to the Physics Department at IIT Indore for providing the requisite facilities for my work. My appreciation extends to my fellow lab mates from the Advanced Energy Material and Devices (AEMD) research group and the Nanoarchitecture Research Group (NRG) at IIT Indore. I would be remiss if I didn't mention Ms. Aayushi Miglani, whose immense assistance during the project was beyond invaluable. Last but certainly not least, I feel blessed and truly privileged to have such wonderful friends as Tarun, Uttam, Hitesh, Laksha, Anurag, Palzor, Kapil, Joginder, Satya, Vikash, and Debankan. Their scientific insights and moral support were pillars of strength during challenging times. Together, we created a wealth of joyous memories. Despite the distance from my family, they ensured that I always felt at home during my tenure.“

Kumar Saumya

Abstract

This thesis presents a detailed analysis of hybrid halide perovskite solar cells (PSCs), a rising PV technology with the potential to exceed traditional silicon-based solar cells in cost-effectiveness, efficiency, and manufacturability. Utilizing a simulation-driven approach, it explores light management and charge transport within the perovskite solar cell stack. The Transfer Matrix Model (TMM) and Drift-Diffusion Model (DDM) are used with experimental data to reveal important findings.

The TMM Python code facilitates optical analysis of the multilayer PSC stack, providing insights into light capture and optical losses. We modified the TMM code to deduce the External Quantum Efficiency (EQE) and idealized short-circuit current density (Jsc) for different architectures and materials. Further to address the shortfalls of TMM, the SCAPS-1D simulation tool, based on the DDM was used to simulate open-circuit voltage (Voc), fill factor (FF), and Power Conversion Efficiency (PCE) for the cells. This broadens our understanding of photovoltaic parameters' dependence on factors like layer thickness, defect density, and more. A key finding is a positive correlation between PCE and dopant density in the active perovskite layer beyond a certain doping density threshold.

Moreover, an n-i-p architecture PSC was fabricated, achieving Voc close to 1V, Jsc of 23.75 mA/cm2, a Fill Factor of 28%, and PCE of 6.5%. Despite Voc and Jsc aligning closely with the simulated results, the fill factor was lower than expected. Drift-diffusion simulation identified the cause of this underperformance as poorly oxidized Spiro-OMETAD.This research emphasizes the crucial role of experimental investigations in validating and refining theoretical models. It also advocates the integration of the TMM model within the DDM framework for comprehensive PSC analysis. These approaches guide the optimization of PSCs, bridging the gap between theory and experiments.

Contents

List of Figures

Chapter 1

Introduction

Solar cells, widely recognized as devices that utilize the photovoltaic effect to convert light energy into usable electric power, were initially documented by Charles Fritts in 1883 [1] and later employed for space applications by Bell Labs during the 1950s [2]. Solar Cells can be made of just a p-n homo- junction of light-absorbing materials (single-junction) or several homo/hetero junctions (called multi-junctions) to exploit maximum light harvesting. The first generation of solar cells is represented by crystalline (mono/poly) silicon solar cells, which have been extensively studied for over five decades. These cells have achieved significant dominance in the photovoltaic market due to their remarkable efficiency (approximately 26% for lab scale and around 20% for module) and long-lasting durability [3]. On the other hand, 2nd generation solar cells, including PV technologies employing rare earth elements (e.g. CdTe, $CuIn_xGa_{(1-x)}Se_2$, GaAs) or amorphous silicon, are categorized as thin-film solar cells. Unlike mono/poly-silicon, which typically measures around 200 - 500 µm, thin-film solar cell thickness fall in the range of 0.4 – 10 µm. As a result, these solar cells are lighter than crystalline silicon while delivering a higher power output per unit weight [4][5]. Currently GaAs Solar cells have shown a record efficiency of 28.8% for single junctions but they are more commonly used in multijunction and concentrated on space applications as these are expensive for domestic deployments[6]. The 3rd-generation of solar cells encompasses a range of technologies that exhibit the potential to achieve both

high efficiency and cost-effectiveness. This group includes dye/quantum-dot sensitized solar cells (D/QD-SSC), organic photovoltaics (OPV), and the more recent halide-perovskite solar cells (PSCs). Over the past decade, perovskite solar cells have garnered considerable interest because of their remarkable power conversion efficiency (PCE), affordability in production, and the ability to tune their bandgap for specific applications [7] [8].

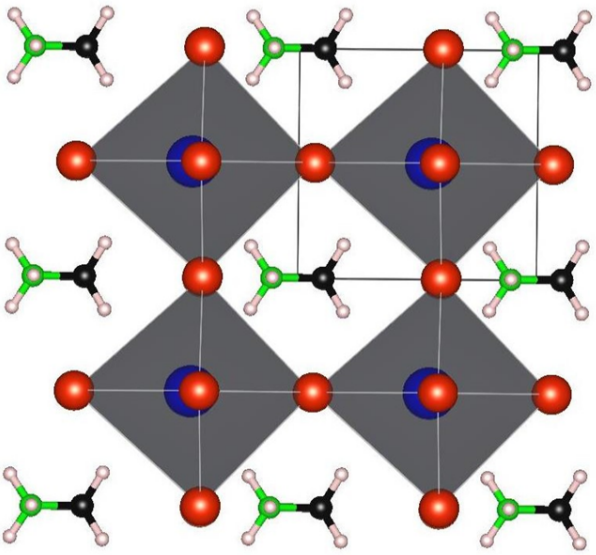

Figure 1.1: Schematic of typical hybrid-halide perovskite ABX_3 structure. Here, MA^+ molecule occupies the A^+ site while the Pb^{2+} sits at B^- site (blue spheres), and the X^- site by I^-(red spheres)

The PSCs have shown remarkable progress in recent years with rapid increases in efficiency, from about 3.8 % in 2009[9] to over 25.6 % [10] to date. While perovskite solar cells have become highly efficient quickly, several challenges such as increasing efficiency at module scale, interface engineering, degradation, and stability of solar cells are still to be tackled[11].

1.1 Hybrid Halide Perovskite

The Halide Perovskite materials are used for the absorber layer of our PSCs as absorption of light leads to the generation of excitons (and free carriers thereafter), later the charge carriers diffuse to the respective transport layers creating the directional flow of electrons and holes in the

opposite direction. Among Hybrid Halide Perovskite materials methyl ammonium lead halide perovskites ($CH_3NH_3PbI_3$)) is the first composition to be extensively studied and have shown remarkable photovoltaic properties due to their remarkable optical and electronic properties i.e. optimal band gap, high carrier mobility, high absorption coefficients, and long diffusion lengths[12] [13] [14]. The structure of $CH_3NH_3PbI_3$ undergoes a transition from a tetragonal form to a cubic one when the temperature reaches 54 °C and it is assigned to the free rotation of MA^+ within the PbI_2 cage making it structurally more symmetric at high temperature than the room temperature configuration. Importantly, its energy gap ranges between 1.5 and 1.6 eV which is suitable for broad-band solar spectrum harvesting in PV applications. [15] [16]. The incorporation of different cations at A, B, and anions at the C sites has shown an advancement of PSC in terms of PCE, stability, and toxicity. Although not any compositional mixing can lead to stable homogeneous compounds only a certain number of cations and anions can be used for this purpose, based on charge neutrality, ionic size, and geometrical tolerance factor $t = \frac{r_a + r_x}{\sqrt{2}(r_b + r_x)}$ [17].

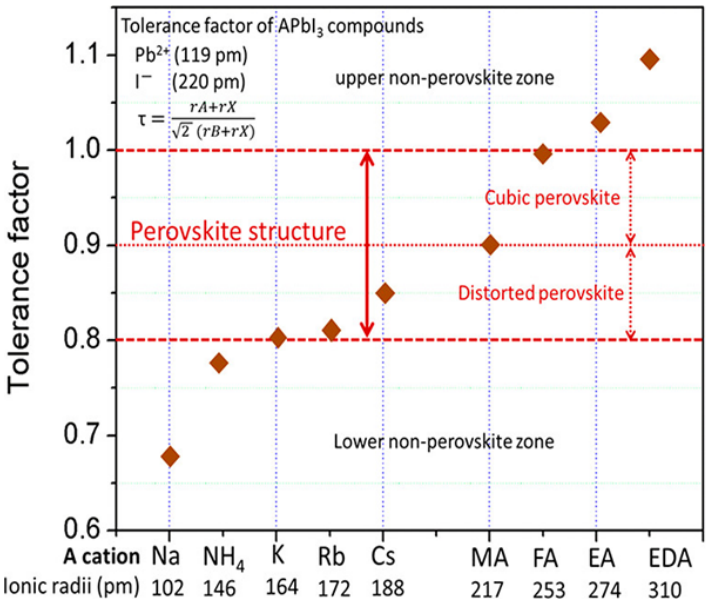

Figure 1.2: Calculated Tolerance factor for different A-site cations [11]

For a compound to assume a perovskite configuration, the tolerance factor should lie between 0.8 and 1.0 [18] [19]. It has been theoretically reported that 742 combinations are possible which can crystalize in per-

ovskite structure [20]. However, the applicability of composition in photovoltaic devices depends on parameters such as band gap, carrier diffusion length/carrier lifetime, conduction and valance band levels, and other processing/morphological limitations. For MA-based perovskite, the tolerance factor is 0.91 and 1.06 depending upon its phase (tetragonal vs cubic). The various attempts to incorporate the dopants/additives at different sites of $MAPbI_3$ have different effects on stability and performance. Since organic cations like MA and FA are naturally hygroscopic, doping with inorganic cations is quite important. While doping at X anion leads to greater thermal stability. Therefore doping at A and X sites with other cations and anions has shown water resistivity and an increase in the electronic and optical properties of PSCs.

1.2 Device Architecture

PSCs typically consist of an Electron Transport Layer (ETL), a light-absorbing hybrid halide perovskite layer, a Hole Transport Layer (HTL), and the two collection electrodes. The PSC's configuration is dictated by the arrangement of the transport layers. In the n-i-p structure, the ETL is deposited first, followed by the absorber layer and the HTL. Conversely, in p-i-n PSCs, the HTL is deposited first, and incident light interacts with the HTL before reaching the absorber layer. The two device schematics are illustrated in Figure 1.3.

1.2.1 Hole Transport Layer (HTL)

The Hole Transport Layer (HTL) plays a pivotal role in ensuring the effective extraction and transportation of photogenerated holes from the photoactive (perovskite) layer to the top metal electrode. The selection of the HTL material hinges on various parameters, such as hole mobility, alignment of HOMO level vis-à-vis perovskite valance band, stability, and suitability with the device fabrication process. Current research endeavors include creating innovative HTL materials and fine-tuning their properties

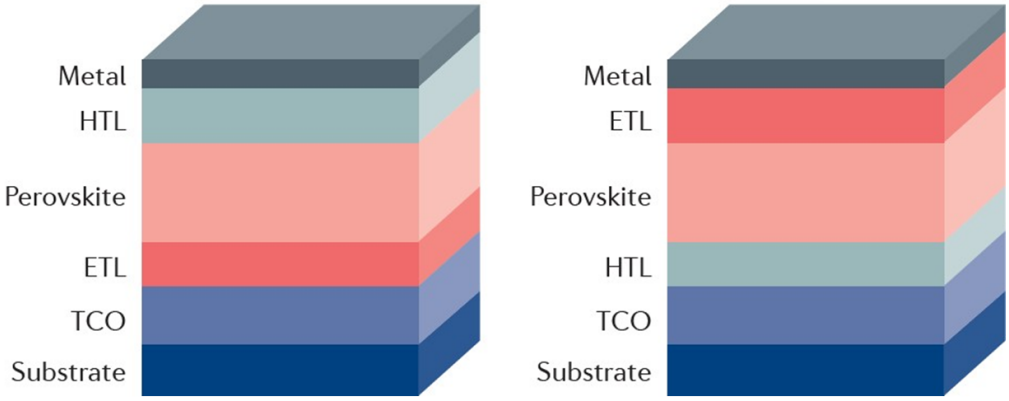

Figure 1.3: Shematic of different archietecture commomly used in PSCs[21] a. NIP Architecture b. PIN Architecture.

to improve the efficiency, stability, and scalability of PSCs [11]. In our research, we utilized spiro-OMeTAD HTL, as it exhibits superior performance and stability as an HTL material in PSCs, owing to its superior hole mobility, low trap density, chemical stability, wide bandgap, and efficient ability to extract and transport holes from the perovskite absorber layer. Several materials are commonly used for HTLs in perovskite solar cells, including spiro OMeTAD, PEDOT: PSS, CuSCN, NiO_x, CuI, and more. The choice of HTL varies depending on the selected configuration and perovskite materials.

1.2.2 Electron Transport Layer (ETL)

In PSCs, Electron Transport Layers (ETLs) are of paramount importance, chiefly due to their role in charge extraction. The ETL is pivotal for the extraction and transportation of photo-induced electrons and functions as a vital component in suppressing charge recombination, acting as a hole-blocking layer, which in turn boosts the overall efficiency of photovoltaic devices. A key requirement of the ETL is a high level of transparency in the UV-Visible region to allow for unhindered passage of photons, which are then absorbed by the perovskite absorber. Furthermore, excitons generated by light absorption in the perovskite layer must be dissociated for collection, either by the ETL or HTL. Several materials have been stud-

ied and employed as ETLs in perovskite solar cells, including TiO_2, ZnO, SnO_2, PCBM (Phenyl-C61-butyric acid methyl ester), Tin Oxide (SnO_2), and C60, among others. In NIP architecture perovskite solar cells, SnO_2 is a frequently used ETL material due to its exceptional performance and stability. The high electron mobility, transparency, chemical stability, efficient electron extraction, and compatibility with solution processing techniques make SnO_2 a highly efficient and stable ETL material in perovskite solar cells

1.2.3 Charge Collection Electrode

Gold is a prevalent metal for the top electrodes (also called back-electrode) in PSCs, though its high cost can be prohibitive. Silver presents an economically viable alternative, being approximately 65 times more affordable than gold. However, there's an inherent challenge when utilizing silver electrodes in conjunction with a solution-based fabrication methods of halide perovskites — silver undergoes rapid corrosion (via silver halide formation), manifesting within a few days of the PSC's fabrication. This corrosion deteriorates the stability of the device, leading to discoloration of the electrode and a decline in the cell's efficiency. Consequently, for our study, we elected to use gold as our top-contact.

Typically, the bottom transparent conducting electrode of Perovskite Solar Cells (PSCs) consists of a 1.1 - 1.5 mm thick glass layer coated with 100 – 200 nm layer of a transparent conducting oxide such as Tin Doped Indium Oxide (ITO) or Fluorine Doped Tin Oxide (FTO).

Chapter 2

Theoretical Background and Literature Review

2.1 History

The increasing energy needs and detrimental effects of fossil fuels on the environment have caused people to switch from non-renewable to renewable sources of energy. Renew- able energy is an inexhaustible source of energy. Solar energy is known to be the largest renewable energy resource that can sustain all present and future energy needs. Solar cells are devices that possess the ability for solar to electric power conversion via the photovoltaic effect[22]. The origins of solar cells can be traced back to the mid-19th century's pioneering discovery of certain materials demonstrating an electric signal when exposed to light, by A. E. Becquerel. His experiments with electrolytic cells and light laid the foundation for future solar cell development. In 1883, Charles Fritts, an inventor from the United States, developed the inaugural functioning solar cell. He achieved this by employing selenium, a type of semiconductor material, and overlaying it with a fine film of gold. Despite the relatively low energy conversion efficiency, this creation represented the initial feasible instance of transforming light into electrical energy [23]. Although the conversion efficiency was low, it marked the first practical demonstration of converting light into electricity. Albert Einstein also published his groundbreaking paper

on the photoelectric effect, which provided a theoretical explanation of how light interacts with matter at the atomic level in 1905 [24]. This work laid the foundation for understanding the fundamental principles underlying solar cell operation. During the 1960s-1980 period, researchers made significant advancements in solar cell efficiency and started exploring different materials and technologies. Silicon solar cells became more efficient, and amorphous silicon and thin-film solar cells were introduced, allowing for flexible and lightweight applications [25]. Solar cell manufacturing also began to scale up, and commercial production of solar panels started. In recent decades, solar cell technology has witnessed rapid growth, driven by increased efficiency, technological advancements, and cost reduction. The development of new materials, such as thin-film solar cells, PSCs, and OPVs, has expanded the possibilities for solar energy generation. Solar panels have become more affordable and are increasingly being adopted for residential, commercial, and utility-scale applications worldwide.

2.2 Global situation of Solar cells

The global situation of PV panels is dynamic and it is, driven by technological advancements, policy support, cost reduction, and environmental considerations. Solar energy is increasingly recognized as a vital component of the global energy transition towards a cleaner, more sustainable future. The global installed capacity of solar photovoltaic systems has steadily increased from the 1990s onwards. The International Energy Agency (IEA) estimated that the cumulative installed capacity of PV exceeded 773 gigawatts (GW) by the end of 2020. Several countries, including China, the United States, India, and European nations, have witnessed significant growth in solar installations. Over time, there has been a substantial decline in the cost of solar cells and PV systems, resulting in increased competitiveness of solar energy compared to conventional energy sources. This cost reduction can be attributed to factors such as economies of scale, advancements in technology, enhanced manufacturing

efficiency, and supportive policy measures. Falling costs have facilitated the widespread adoption of solar energy across residential, commercial, and utility-scale applications. Several global governments have enacted diverse policies and incentives to foster the widespread use of solar cells (ref). Among these are feed-in tariffs, tax benefits, subsidies, and set goals for renewable energy. The intention behind these strategies is to encourage investments, generate employment opportunities, curb greenhouse gas emissions, and promote diversity in energy resources. There have been significant advancements in PVs to boost efficiency, durability, and versatility. Traditional silicon-PV continues to dominate the PV market, but RD efforts are also being carried out on emerging -PVs such as PSCs, OPVs and their tandem architectures with silicon solar cells. These technologies offer potential advantages, such as higher efficiency, lower costs, and greater flexibility. De- spite the growth and advancements, challenges remain in the solar cell industry. These include the intermittent availability of solar power, grid integration issues, manufacturing, stability and recycling processes, and resource constraints. However, such challenges also present opportunities for innovation, research, and collaboration to address these issues and further improve the performance and sustainability of solar cells.

2.3 Solar irradiance

Solar irradiance describes the amount of solar power per unit area received at a specific location on Earth's surface. Solar irradiance data is important for various applications, including solar energy system design, climate modeling, agriculture, and weather forecasting. Measurement and estimation of solar irradiance are conducted using instruments such as pyranometers, pyrheliometers, and satellite-based radiometers. These instruments provide valuable data for understanding the solar resource and optimizing the performance of solar energy systems. The atmospheric parameters have an impact on solar radiation as it reaches the surface of the Earth, affecting its distribution and intensity. The angle of incidence at

which radiation enters the atmosphere determines the amount of radiation that reaches the surface. As the route length increases, there is greater attenuation, resulting in reduced radiation reaching the surface. This attenuation is defined as :

$$AM = \frac{1}{cos(\phi_{sun})} \tag{2.1}$$

where ϕ_{sun} is the angle of elevation of the Sun also known as the zenith angle. Different Air Mass values, such as AM 0, AM 1.0, AM 1.5, etc., represent specific Sun angles and path lengths. These values are used to characterize and standardize solar energy measurements, device testing, and performance evaluation in the field of photovoltaics and solar energy research. The typical spectrum taken into account for PV applications is AM1.5G, which corresponds to the zenith angle of 48.2°.

2.4 Fundamentals of solar cells

Photovoltaic cells (or solar cells), transform incident solar power into electrical power through an effect called the photovoltaic effect. The working of a PV cell can be described as a combination of the following processes:

Absorption of incident radiation and generation of e-h pairs: The fundamental building blocks of solar cells are semiconductor materials, which harness the energy of photons via absorption to create electron holes provided the energy of incident photos is greater than the band-gap of semiconductor used in PV. Indeed, the band gap of the semiconductor and its wavelength-dependent absorption coefficients for the sunlight plays crucial roles in this process. Furthermore, for every photon absorbed by the semiconductor, its energy is utilized in the excitation of an electron (e-) from the valence to the conduction band leaving behind a hole (h+) in valence bad. Such electron-hole pair generation is pivotal to the working of a PV device.

1. Absorption of Photons: Solar cells are made of semiconductor materials. When photons (particles of light) from sunlight strike the semi-

conductor material, they can be absorbed by the atoms in the material. The energy from the photons is transferred to electrons in the atoms, exciting them to a higher energy state (or band in semiconducting solids).

2. Separation of Charges: In a typical PV device, the depletion region formed out of the p-n junction possesses a built-in electric field that causes the directionally opposite flow of photogenerated electrons and holes causing the excitons (bound e-h pair) to dissociate and then drift in opposite directions. This separation prevents the recombination of the charges. This directional flow in opposite directions prevents there combination of the photo-generated charges.

3. Collection of Electrons and holes: Metal contacts, typically made of silver/ aluminum or transparent conducting oxides (TCO), are placed on the top and bottom of the semiconductor material. These contacts allow the free (e^-) and (h^-) to flow opposite directions and constitute the photocurrent. The top contact is usually a grid-like structure to maximize light absorption and minimize shading.

4. Flow of Current: When a load, such as an electrical circuit/appliance, is connected to the solar cell, the separate photo-generated electrons and holes flow through the external circuit, to constitute the photocurrent in a PV device.

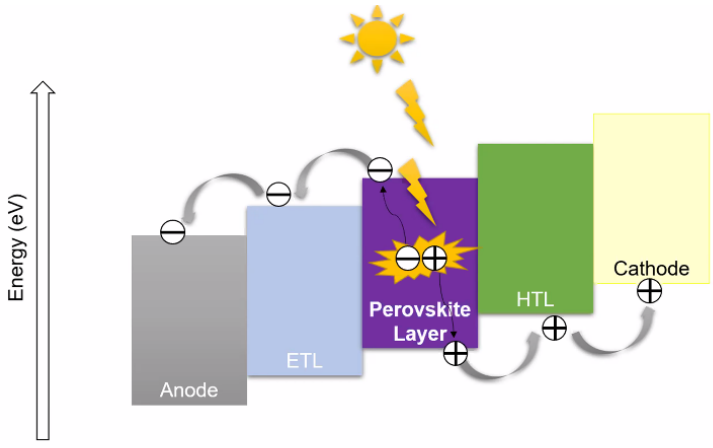

Figure 2.1: Schematic of Energy alignment between different components of PSCs

The PV output is a function of several interdependent parameters

such as the semiconductor material properties, cell design, and environmental conditions. Researchers and engineers continually work on improving solar cell efficiency by optimizing materials, cell architectures, and manufacturing processes. These solar cells are typically combined into solar panels or modules to provide higher power outputs. Multiple modules can be connected to form a solar array, which can generate significant amounts of electricity for residential, commercial, or utility-scale applications.

2.5 Perovskite solar cell specific

Recently significant advancements have been achieved in architectural design, cost-efficient fabrication methods, and material selection, contributing to enhanced efficiency, stability, and scalability of PSCs. Transformational changes and improvements have been brought since their inception. Solid-state Dye-Sensitized Solar Cells (SS-DSSCs) formed the basic architecture of PSCs. In SS-DSSCs, a layer of porous nanoparticles adsorbed by a light-absorbing dye serves as the light-harvesting material. This dye absorbs photons, leading to the creation of electron-hole pairs that are subsequently transported through the porous layer and an HTL to the respective electrodes. A typical SS-DSSC has a sandwich-like structure featuring a Transparent Conductive Oxide (TCO) layer as the anode, a dye-sensitized layer, and an HTL serving as the hole-conducting medium.

However, to address the limitations posed by the low light harvesting ability of dyes in SS-DSSCs, researchers shifted their focus towards hybrid halide-based perovskite light-harvesting layers [26]. This design offered enhanced power conversion efficiency due to better light harvesting properties of hybrid halide perovskites over the typical dyes used in SS-DSSC [27].

Further innovation led to the PIN (inverted) configuration of perovskite solar cells. This configuration inverts the order of the layers compared to the traditional NIP (n-type/intrinsic/p-type) structure, enabling better electron extraction and providing a more efficient charge transport pathway, resulting in improved device performance. Despite the promising

prospects of PSCs, there are several challenges (listed below) that need to be addressed before these cells can be commercialized.
several challenges need to be fixed for their commercialization. These include:

2.5.1 Stability of PSCs

As the efficacy of PSCs consistently surpasses the 25% mark, its durability is another significant issue to address. This affects their overall functionality over the long term, causing a reduction in both efficiency and reliability. Researchers have shown that the operational longevity of PSCs' is compromised by moisture, oxygen, and heat, causing them to deteriorate. The specific stressing points affecting the stability of PSCs are discussed in more detail below,

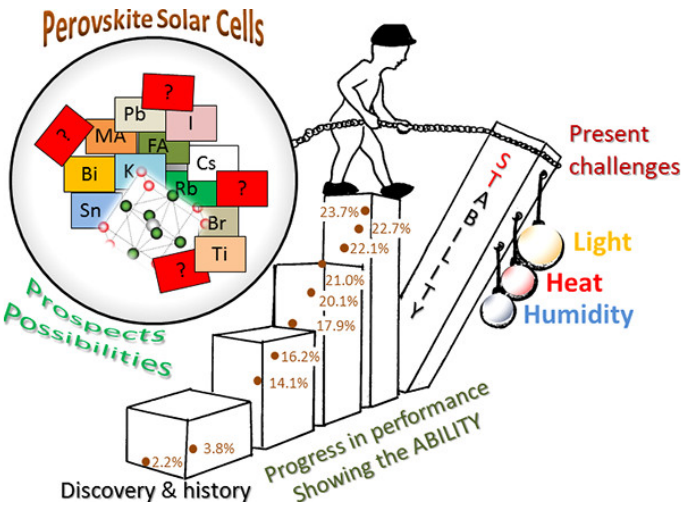

Figure 2.2: Shematic illustrating different factors influencing the stability of PSCs[11]

Humidity: Hybrid Perovskite materials are highly sensitive to moisture, as organic cations used at the A site of perovskite are quite hygroscopic[28] in nature causing structural changes, ion migration, and chemical reactions within the cell. Exposure to humid conditions can lead to the degradation of the perovskite layer and the formation of undesired phases, resulting in reduced efficiency and stability [29]. Researchers have tried to reduce its effect by inducing Encapsulation, Moisture Barrier Layers and Interfacial Engineering [30].

Heat: Perovskite solar cells can degrade under prolonged exposure to intense light and elevated temperatures. High-energy photons can induce photochemical reactions, while excessive heat can accelerate material degradation and lead to thermal instability [31]. These factors cause the deterioration of the halide perovskite, loss of crystallinity, and low performance.

Ion Migration: Perovskite materials are susceptible to ion migration, which can occur under an applied electric field or environmental stress. Ion migration can cause charge imbalances, affect charge transport properties, and induce device degradation over time. Experimental results prove that Halides easily show ion migration in PSCs [32]. For e.g. the incorporation of inorganic cation like Potassium (K) has shown the suppression of ion migration [33].

Interface Degradation: The interfaces between the different layers in the perovskite solar cell, such as the perovskite/electron transport layer and perovskite/hole transport layer interfaces, are prone to degradation. Interface reactions, interdiffusion of materials, and charge recombination at the interfaces can lead to performance deterioration [34]. Several strategies are employed to prevent or minimize interfacial degradation in perovskite solar cells: Interfacial Passivation, Encapsulation and Moisture Barrier Layers etc. [35]

2.5.2 Lead Toxicity

Lead toxicity is a serious hazard with PSCs that can severely affect health as well as the environment. World Health Organization (WHO) is also making strict policies against Lead (Pb). Studies have indicated that the complete replacement of lead in perovskite solar cells (PSCs) results in a decline in their performance [36], as the properties exhibited by lead are highly suitable for photovoltaic applications [37]. To deal with this problem there are various ways in which researchers have tried to reduce its content and its leakage. The partial replacement of Pb has shown an increase in performance. Some alternatives being explored include using

tin (Sn), bismuth (Bi), Germanium (Ge), or other non-toxic elements in the perovskite structure. Another efficient strategy to reduce Pb leakage can be through introducing lead-absorbing materials to capture Pb^{2+} ions the process known as chemisorptions [38]. While using such an absorbing agent it should be chosen in such a way that it doesn't affect the overall performance of PSCs.

Chapter 3

Transfer Matrix Model

3.1 Introduction

Transfer matrix modeling is used to understand the transmission and reflection of electromagnetic waves through a multi-layer stack. It involves breaking down a multi-layered optical structure into individual layers and representing each layer using a transfer matrix. Conventionally calculating Fresnel coefficients at each layer of the structure is practically very difficult to do. A transfer matrix is a mathematical tool that describes electromagnetic fields that change as they pass through the layer. Transfer matrix modeling is a versatile technique that can be applied to several optical structures. It allows the optimization and designing of optical devices for specific applications, such as anti-reflection coatings, color filters, and optical sensors. It provides a rigorous mathematical framework for studying the behavior of electromagnetic waves in complex optical systems and enables the development of novel optical devices for various applications. Overall, transfer matrix modeling uses the mathematics of matrices and complex numbers to describe the propagation of electromagnetic waves through thin-film structures. It offers a potent tool for analyzing and designing optical devices, making it extensively utilized in the field of optics and photonics.

3.2 Mathematics of Transfer Matrix Model

The transfer matrix of a thin-film layer is described in the form of a matrix that relates the amplitude of the reflected and transmitted waves to the amplitude of the incident wave. It depends on the thickness of the layer, the refractive index of the layer, and the angle of incidence of the incoming wave. Calculation of the transfer matrix involves applying the Fresnel equations, which elucidate the characteristics of electromagnetic waves at the interface of two media having distinct refractive indices. After obtaining the transfer matrix for each layer, the collective transfer matrix of the multi-layered structure can be acquired by multiplying the individual transfer matrices in succession. The resulting transfer matrix describes the transmission and reflection of the wave through the entire structure.

3.2.1 Matrix at multiple interfaces of multi-layer structure

For a multi-layered structure, the incident Electric field is taken at the side of the illumination and the calculations are done at each interface. To do this we only require the optical constants of each material of a multi-layer architecture. Let us suppose the electromagnetic wave pass from one material to the other at two interfaces dividing three materials separately. Taking the Electric field into consideration (for simplicity).
Now we will establish the relationship between the incoming layer 1 and outgoing layer 3 Electric fields.

$$n(x) = \begin{cases} n_1 & x < 0 \\ n_2 & 0 < x < d \\ n_3 & x > d \end{cases}$$

The z component of the wave-vector kz=β does not change throughout the problem (a consequence of phase continuity). Therefore it causes

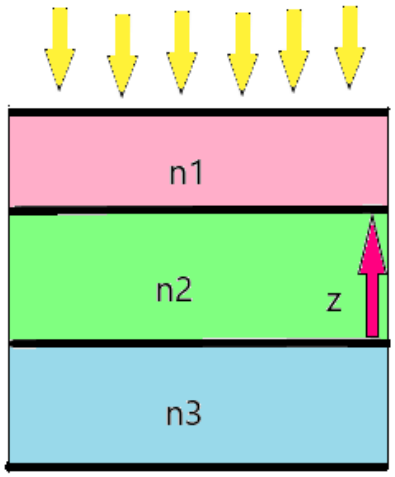

Figure 3.1: Electric field in multilayer stack

a simple dependence on the progress in z direction:

$$E = E_o i e^{(iwt - i\beta z)} \tag{3.1}$$

Now we would like to find a general way to relate any pair of electric and magnetic field amplitudes in any layer to those in any other layer.

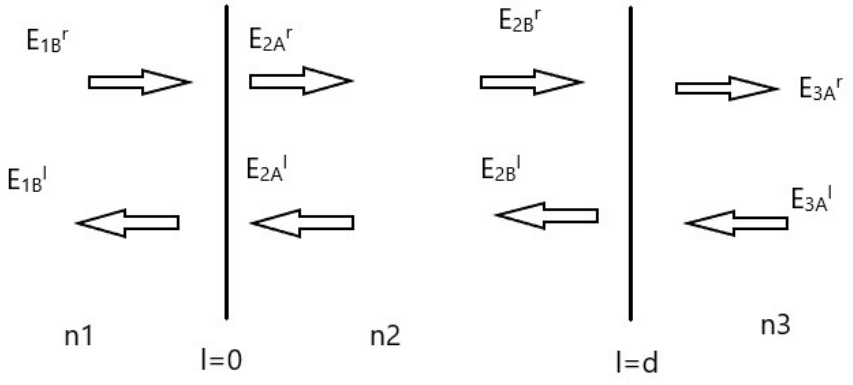

Figure 3.2: Electric field at 2 interfaces of multilayer heterojunction

Here A and B indices are helping us to find fields inside two interfaces. Let's start writing the relation from the n_2 and n_3 interface.

$$\begin{bmatrix} E_{2B}^r \\ E_{2B}^l \end{bmatrix} = D_{23} \begin{bmatrix} E_{3A}^r \\ E_{3A}^l \end{bmatrix} \tag{3.2}$$

where D is a transmission matrix (described below). Inside material n_2.

$$\begin{bmatrix} E_{2A}^r \\ E_{2A}^l \end{bmatrix} = P_2 \begin{bmatrix} E_{2B}^r \\ E_{2B}^l \end{bmatrix} \tag{3.3}$$

At interface n_1 and n_2.

$$\begin{bmatrix} E_{1B}^r \\ E_{1B}^l \end{bmatrix} = D_{12} \begin{bmatrix} E_{2A}^r \\ E_{2A}^l \end{bmatrix} \tag{3.4}$$

substituting equation 6 and 7 in 8^{th} equation. Now for the propagation of waves in between the interfaces of thickness 'd' we have a Propagation matrix.

$$P_{01} = \begin{bmatrix} e^{i\zeta d} & 0 \\ 0 & e^{-i\zeta d} \end{bmatrix} \tag{3.5}$$

where $\zeta = \frac{2\pi n}{\lambda}$ To find the relation between layer 1 and layer 3 and putting all the above relations we will get

$$\begin{bmatrix} E_{1B}^r \\ E_{1B}^l \end{bmatrix} = D_{12}P_2D_{23} \begin{bmatrix} E_{3A}^r \\ E_{3A}^l \end{bmatrix} \tag{3.6}$$

Here $D_{12}P_2D_{23}$=M (Transfer Matrix).

- for only Three Materials or Two interfaces.

$$\begin{bmatrix} E_{incident} \\ E_{reflected} \end{bmatrix} = M \begin{bmatrix} E_{transmitted} \\ 0 \end{bmatrix} \tag{3.7}$$

$$E_{incident} = M_{11}E_{transmitted} \tag{3.8}$$

$$E_{reflected} = M_{21} E_{transmitted} \tag{3.9}$$

From above Equation

$$t = \frac{E_{transmitted}}{E_{incident}} = \frac{1}{M_{11}} \tag{3.10}$$

$$r = \frac{E_{reflected}}{E_{incident}} = \frac{M_{21}}{M_{11}} \tag{3.11}$$

we also know that the reflection and transmission coefficient depends upon the refractive indices of the materials.

$$r_{12} = \frac{E_r}{E_i} = \frac{n_1 - n_2}{n_1 + n_2} \tag{3.12}$$

$$t_{12} = \frac{E_t}{E_i} = \frac{2n_1}{n_1 + n_2} \tag{3.13}$$

$$D_{12} = \begin{bmatrix} r_{12} & t_{12} \\ t_{21} & r_{21} \end{bmatrix} \tag{3.14}$$

Similarly transmission matrix can be written for second interface can be written.

3.3 Simulation work on Transfer Matrix Modeling

The Macghee group at Stanford University has published a Python-based programming code to find out the optical properties of a multi-layer stack and other parameters. In this work, the simulation has been used to understand the Light management inside the Perovskite Solar Cells. This simulation pakage already contains the light absorbance, normalized electric field, and generation rate of each layer of a multi-layer structure but some figures of merits were missing in it. Subsequently, I introduced some specific equations into the code (details provided below), enabling the incorporation of the Generation Rate as a function of wavelength This addition

facilitated the calculation of the External Quantum Efficiency, a critical parameter often employed to evaluate the performance of various photovoltaic devices and to fine-tune the design and manufacturing processes of novel devices.

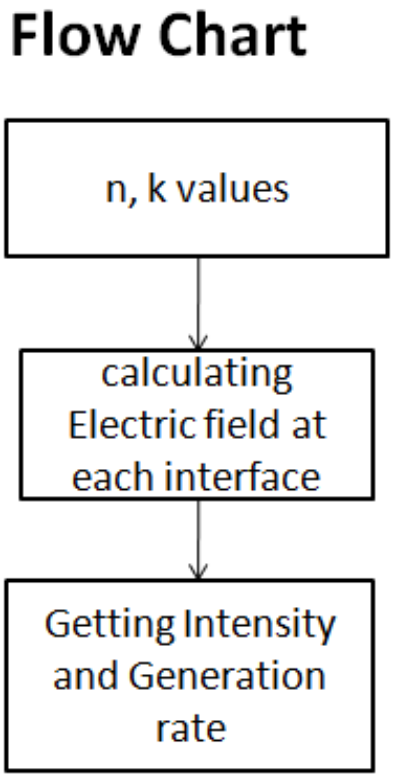

Figure 3.3: Flow chart of the TMM simulation.

The electric field inside of any layer i at any given location is expressed in terms of the electric field of the incident wave by

$$E_i(x) = E_i^+(x) + E_i^-(x) = [t_i^+ e^{i\zeta x} + t_i^+ e^{i\zeta x}]E_0^+ \tag{3.15}$$

3.4 Formulations of TMM Simulation

Using this $E_i(x)$ of above section, we can calculate following parameters. The **time averaged power** (The time-averaged power output is the average power that the cell generates over a period of time.) can be calculated as:

$$Q_i(x) = \frac{4\pi\epsilon c k_i n_i \mid E_x \mid^2}{2\lambda} \tag{3.16}$$

From this time averaged power we can find the **generation rate** as a function of position in the device by solving the exciton diffusion equation of each layer i [39]. The generation rate determines the rate at which charge carriers (electrons and holes) are created and thus assumes a vital role in defining the device performance. The generation rate holds significant importance in the design and optimization of solar cells since it establishes the maximum threshold for the electrical current that can be generated by the device. By improving the generation rate through the use of materials with higher absorption coefficients, better light trapping and coupling structures, and improved device architectures, researchers can improve the overall efficiency and performance of solar cells.

$$G_i(x) = \frac{\lambda Q_i(x)}{hc} \tag{3.17}$$

Now this generation rate can be integrated to all positions at a single wavelength to find out the generation rate as a function of wavelength.

$$G(\lambda) = \int G_i(x)\, dx \tag{3.18}$$

External Quantum Efficiency (EQE) : QE is a metric that quantifies the ratio of electrons collected from a PV cell to the number of incident photons for a particular wavelength. The EQE is typically expressed as a percentage or a fraction, and it can vary with the incident wavelength. The EQE of a solar cell is an important parameter that characterizes its performance. It provides information about the fraction of absorbed photons that are converted into electrical current.

The EQE is measured experimentally by illuminating the solar cell with monochromatic light of a specific wavelength and intensity and then measuring the corresponding photocurrent generated by the cell. The incident photon flux is calculated from the known spectral irradiance of the light source, and the EQE is then determined as the ratio of the photocurrent to the incident photon flux. This generation rate can be divided by the photon flux ($\phi(\lambda)$) (taking its units into consideration).

$$EQE = \frac{G(\lambda)}{\phi(\lambda)} \tag{3.19}$$

Short circuit Current Density(J_{sc}) The short-circuit current density (J_{sc}) represents the maximum current density that can be generated by the solar cell under short-circuit conditions, i.e when the output terminals of the cell are connected together with a wire of negligible resistance, resulting in zero voltage across the terminals. J_{sc} is an important parameter in solar cell performance, as it sets the upper limit for the photocurrent that can be generated by the cell.

J_sc from generation rate G(x):

$$J_{sc} = \frac{1}{q} \int G(x), dx \tag{3.20}$$

J_sc from External Quantum Efficiency (EQE):

$$J_{sc} = q \int EQE(\lambda), \phi(\lambda), d\lambda \tag{3.21}$$

By understanding and optimizing the factors that affect the EQE, J_sc, generation rate, and absorbance, researchers can improve the overall efficiency and power output of solar cells.

This model is very much successful to understand the light management of a multilayer stack. But it doesn't take into consideration of defect densities of the materials, interfacial densities, and charge transport properties of the structure. Hence it can't give the electrical results and certain figures of merits i.e. V_{oc}, Fill Factor, and Efficiency of the solar cells. That's why it's required to study a model which takes all these factors into consideration and gives all the figures of merits of solar cells. Drift Diffusion Model is the smartest way to deal with this.

Chapter 4

Drift Diffusion Model

4.1 Introduction

The Drift Diffusion model offers a mathematical structure that elucidates the conduct of charge carriers, namely electrons and holes, in semiconductor materials under the impact of electric fields. This model encapsulates two primary principles governing the charge carriers' motion in semiconductors: drift and diffusion. Drift delineates the motion of charge carriers as they respond to an electric field. It transpires when a charge carrier is subjected to a force in the direction of the electric field, leading to its movement along a trajectory defined by the electric field. Contrarily, diffusion signifies the stochastic movement of charge carriers triggered by the concentration gradient and thermal energy, causing them to move in a direction independent of the electric field's alignment. The Drift Diffusion model amalgamates these processes, thereby depicting the comprehensive behavior of charge carriers in semiconductors. This model is typically employed to scrutinize and architect semiconductor devices such as diodes, transistors, and solar cells. It holds substantial utility in the semiconductor industry, facilitating the design and numerical analysis of diverse electronic devices.

4.2 Mathematics of Drift Diffusion Model

The DDM in semiconductor physics is typically expressed through a set of partial differential equations (PDEs) that describe the behavior of the electron and hole densities, as well as the electric potential and current density. The specific equations and parameters used in the model depend on the specific semiconductor device and operating conditions being studied. In the drift Diffusion model, we use Electrotromagnetic equations along with certain boundary conditions to describe the Electric field inside the device.

$$E = -\nabla.\phi \tag{4.1}$$

$$J_n = -eD_n\nabla n - e\mu_n n.E(x,t) \tag{4.2}$$

$$J_p = qD_p\nabla p + q\mu_p p.E(x,t) \tag{4.3}$$

where μ_n, and μ_p stand for electron and hole mobilities, E(x,t) is the electric field, and Dn and Dp are the electron (hole) diffusion coefficients. q stands for the elementary charge, n, and p for the electron/hole density.

The 1st part of equations 3.2 and 3.3 indicates that the Electron and hole current densities are created by Diffusion and Drift of the carriers respectively. That's why The field equations (3.1, 3.2, 3.3) are known as charge creation equations.

4.2.1 Transport equation

From the charge continuity equation, we know:

$$\nabla.J_n = -\frac{\partial\rho}{\partial t} \tag{4.4}$$

Electron (n) and hole (p) continuity equations in a device are described by the current transport, generation rate G, and recombination R of free charge carriers:

$$\frac{\partial p}{\partial t} = -\nabla.J_p + G_p - R_p \tag{4.5}$$

$$\frac{\partial n}{\partial t} = -\nabla.J_n + G_n - R_n \tag{4.6}$$

The G term represents the free charge carriers' generation caused by the absorption of photons. The term R signifies the recombination-driven losses. The equations encompass all potential mechanisms of generation and recombination losses, accounting for n and p.

$$\nabla.\epsilon\nabla.\phi = -\rho \tag{4.7}$$

4.2.2 Recombination

The occurrence of photocarrier recombination in PSCs is a significant event that can impose constraints on their overall efficiency. When perovskite layers in PSCs are exposed to sunlight, they give rise to electron-hole pairs. Under perfect conditions, these excitons ought to separate into independent electrons and holes, which can then be amassed at the corresponding electrodes, thereby generating an electric current. Nonetheless, charge recombination might transpire before the charges can reach the electrodes, leading to a decrement in the solar cell's efficiency. In perovskite solar cells, a variety of charge recombination mechanisms can be observed:

Radiative recombination: When a photogenerated electron in the conduction band of a semiconductor recombines with its counterpart (i.e. a hole in the valance band) emitting a photon equal to the band gap of the semiconductor it is termed as the radiative recombination. Radiative recombination is desirable in some cases, as it can lead to the emission of photons and their re-absorption within the cell leading to improved EQE of the solar cell. However, excessive radiative recombination can limit the overall device efficiency. Coloumb attraction between the photogenerated e-h pairs generally leads to radiative recombination.

Non-radiative recombination: This involves the recombination of charges without the emission of photons. It occurs through defects or trap states present in the perovskite absorber or at the interfaces between the perovskite layer and the charge transport layers. Non-radiative recombination is considered a dominant loss mechanism in PSC and can significantly reduce their efficiency. Trap-assisted recombinations and Auger recombination fall into this criteria.

Trap-assisted recombinations This is a form of recombination wherein a charge carrier (either an electron or hole) is captured by a trap state. This trap state functions as an intermediate energy level nestled between the conduction and valence bands. The trapped carrier may remain trapped for a duration of time before it either recombine with another carrier or gets released from the trap to a lower energy/band. Under equilibrium, this rate can be expressed as [40]

$$R = \frac{C_n C_p N_t (n.p - n_e p_e)}{C_n(n + n_e) + C_p(p + p_e)} \tag{4.8}$$

here C_n and C_p are the capture cross-sections for electrons and holes, N_t is the density of traps, and n and p are electrons and hole densities respectively. n_e and p_e are the density of free electrons and holes in equilibrium.

Coloumb attraction leading to recombinations The Coulomb attraction between the e-h pair facilitates their recombination. The Coulomb attraction causes the electron and hole to approach each other, and when they come close enough, they can recombine. The recombination process involves the annihilation of the e-h pair, resulting in the neutralization of their charges. This process releases energy in various forms depending on the type of recombination, such as radiative recombination or non-radiative recombination.

$$R = \frac{e(\mu_n + \mu_p)np}{\epsilon_r \epsilon_0} \tag{4.9}$$

Auger recombination Auger recombination is characterized as an event wherein the recombination of a charge carrier, such as an electron

or hole, with another of its kind leads to the redirection of surplus energy towards a third charge carrier, instead of releasing a photon. This type of recombination is generally observed under elevated temperature conditions.

The total recombination in solar cell devices is the sum of all three recombinations described above by combining all these we can substitute it in equations 4.5 and 4.6

4.2.3 e-h pair Generation rate

The generation rate is a crucial parameter in determining the overall efficiency of a solar cell. The generation rate of PSCs has been described in section 3.4. In DDM the Generation rate is expressed as

$$G(\lambda, x) = \alpha(\lambda, x) N_{Photon}(\lambda, x) \tag{4.10}$$

This can be integrated over all wavelengths of incoming photons

$$G(x) = \int_{\lambda_{min}}^{\lambda_{max}} \alpha(\lambda, x) N_{Photon}(\lambda, x)\, d\lambda \tag{4.11}$$

4.2.4 Short Circuit current density ($\mathbf{J}_{sc}$)

The sum of the hole's current density and the electron's current density at zero resistance is the Short Circuit current density J_{sc} described in section 3.4. After putting the Recombination rate from Equation 4.8 and 4.9 generation rate from Equation 4.11 and applying the boundary conditions of electrons and holes charge densities at all interfaces of our PSCs. The total current density can be calculated as

$$J_{sc}(x) = J_n(x) + J_p(x) \tag{4.12}$$

4.2.5 Open Circuit Voltage

Open circuit voltage (Voc) is a key parameter in solar cell characterization and represents the maximum voltage that a solar cell can produce when there is no external load connected to it. It is also referred

to as the maximum voltage output or the voltage at the maximum power point. The open circuit voltage can be affected by various factors, including the bandgap of the semiconductor material, the presence of defects or impurities, and the device design and fabrication process. Higher-quality materials and optimized device structures can lead to higher open circuit voltages.

$$V_{oc} = \frac{KT}{q} log[\frac{J_{sc}}{J_0} + 1] \tag{4.13}$$

where J_{sc}= short circuit current density

J_0= reverse saturation current density

$$J_0 = qni^2(\frac{1}{N_D}\sqrt{\frac{D_p}{\tau_p}} + \frac{1}{N_A}\sqrt{\frac{D_n}{\tau_n}}) \tag{4.14}$$

n_i is the intrinsic carrier concentration in the semiconductor material D_p and D_n are the diffusion coefficients of the holes and electrons, N_D and N_A are the donor and acceptor concentrations at the n side and p side, respectively, τ_n and τ_p are the carrier lifetimes of holes and electrons, respectively.

4.2.6 Fill Factor

The fill factor (FF) serves as a crucial measure in gauging the effectiveness of solar cells, perovskite solar cells included. It ascertains the degree to which a solar cell can proficiently transform incoming light into electric power. The fill factor is essentially the proportion of a solar cell's peak power output to the multiplication result of the open-circuit voltage (V_{oc}) and the short-circuit current (I_{sc})::

$$FillFactor = \frac{P_{max}}{V_{oc} \times J_{sc}} \tag{4.15}$$

$$P_{max} = V_{mpp} \times J_{mpp} \tag{4.16}$$

V_{mpp} = Voltage at maximum power point, J_{mpp} = Current density at maximum power point The fill factor represents the combined effects of the series resistance, shunt resistance, and recombination losses within the solar cell.

A high fill factor indicates low resistive and recombination losses, resulting in better power conversion efficiency. In perovskite solar cells, achieving a high fill factor is crucial for maximizing power conversion efficiency.

4.2.7 Power Conversion Efficiency

Power conversion efficiency (PCE) is a crucial parameter used to assess the performance of a solar cell. It quantifies the ability of the solar cell to convert incident light into usable electrical power. The PCE is calculated as the ratio of the maximum power output of the solar cell (Pmax) to the incident power of the light (Pin):

$$PCE = \frac{P_{max}}{P_{in}} \times 100\% \tag{4.17}$$

P_{in} = incident power of the light. The PCE of a solar cell is influenced by the Absorption of light, Carrier generation Carrier transport Charge separation collection, Voltage, and current.

Chapter 5

Experimental Methods and Procedure

The synthesis of perovskite solar cells involves the preparation of the perovskite materials, ETLs, Spiro, and Electrodes. As discussed above, the architecture we used for the simulation ($FTO/SnO_2/MAPbI_3/Spiro/Au$) is the same one we will investigate experimentally. Before fabricating our solar cell it's important to optimize the perovskite layer also known as the active layer ($MAPbI_3$). Perovskite solar cells are often prepared using solution-based processes due to several advantages offered by this method which include Versatility in Precursor Synthesis, Low-Temperature Processing, Scalability, Cost-effectiveness, Compatibility with Flexible Substrates, and easy mixing of different materials or incorporating additives [41]. Before going to actual fabrication the most important thing is substrate cleaning. Substrate cleaning is crucial for achieving high-quality PSCs with improved efficiency and durability [42]. The substrate should be free from any contaminants, such as dust, oils, grease, or residues, that could interfere with the deposition and quality of subsequent layers. The level of substrate cleaning required can vary depending on the specific fabrication process and the cleanliness standards desired. Generally, a high level of cleanliness is recommended to minimize contamination and optimize the performance of perovskite solar cells. The various steps that have been taken to clean our substrate are described in the section below.

Fabricating PSCs requires careful preparation of the perovskite materials, transport layers (ETL/HTL), and electrodes. As previously outlined, the architecture we simulated (FTO/SnO_2/$MAPbI_3$/Spiro/Au) is the same structure that will be subjected to our experimental investigation. Before we proceed with the fabrication of our solar cell, it's crucial to optimize the perovskite layer, also referred to as the active layer (MAPbI3). PSCs are typically prepared using solution-based processes due to their many benefits. These include adaptability in precursor synthesis, low-temperature processing, scalability, affordability, compatibility with flexible substrates, and the simple integration of various materials or additives. Following, are the steps we adhered to in the process of fabricating perovskite solar cells

Fabricating perovskite solar cells requires careful preparation of the perovskite materials, transport layers (ETL/HTL), and electrodes. As previously outlined, the architecture we simulated (FTO/SnO_2/$MAPbI_3$/Spiro/Au) is the same structure that will be subjected to our experimental investigation. Before we proceed with the fabrication of our solar cell, it's crucial to optimize the perovskite layer, also referred to as the active layer ($MAPbI_3$). Perovskite solar cells are typically prepared using solution-based processes due to their many benefits. These include adaptability in precursor synthesis, low-temperature processing, scalability, affordability, compatibility with flexible substrates, and the simple integration of various materials or additives [30]. Following, are the steps we adhered to in the process of fabricating PSCs.

5.1 Perovskite $MAPbI_3$ optimization

Perovskite layer optimization is of significant importance in the fabrication of perovskite solar cells. The perovskite layer serves as the active light-absorbing material in the solar cell, and its properties directly impact the device's performance. Therefore its optimization is important for better performance, stability, and scalability of PSCs. Optimization efforts focus on improving the crystallinity, morphology, and purity of the $MAPbI_3$ film

to enhance light absorption, charge generation, and charge transport. This leads to higher PCE in PSCs. Here we have optimized the crystallinity and morphology of $MAPbI_3$ thin films. The following techniques are used to enhance the film quality, reduce defects, and improve the charge transport properties. Here's a brief overview of these optimization methods:

Anti-Solvent Quenching: Anti-solvent quenching involves the addition of a non-solvent or anti-solvent to the perovskite precursor solution during the spin-coated step. This process induces rapid and uniform nucleation at the top layer of the spin-coated film, which upon heating leads to larger and uniform crystal grains. Anti-solvents like chlorobenzene, toluene, or diethyl ether are commonly used to promote the nucleation and growth of high-quality perovskite crystals. Anti-solvent quenching helps in achieving improved film morphology, reduced grain boundaries, enhanced crystallinity, and reduced trap densities, leading to improved device performance [43]

Gas Annealing Gas annealing refers to subjecting the deposited perovskite film to a controlled atmosphere of specific gases or vapors. Common gases used for gas annealing include nitrogen (N_2), oxygen (O_2), or a mixture of them. Gas annealing helps in improving the structural and optoelectronic properties of the perovskite film[44]. It can lead to enhanced grain growth, improved crystallinity, reduced defect densities, orientational change, and improved charge transport within the perovskite layer [45]. The gas annealing process can also modify the film stoichiometry and reduce the presence of undesirable by-products, thereby enhancing stability.

In this study, we exposed the perovskite film to a methylamine gas. Studies indicate that methylamine gas can insert itself into the $MAPbI_3$ phase, resulting in a liquid-like state. Once the surplus methylamine gas is eliminated, it can recrystallize into the original solid $MAPbI_3$ phase [46]. This recrystallized film post methylamine treatment has better crystallinity, preferred orientation, and fewer pin-holes than the film that is not subjected to gas annealing

5.1.1 Methodology for $MAPbI_3$ thin film preparation

The $MAPbI_3$ was prepared on a cut glass sheet substrate (2 cm × 2 cm).).The substrates underwent a cleaning process prior to spin coating, involving immersion in an ultrasonic bath for 25 minutes each in a sequence of cleaning solutions: deionized (DI) water with soap solution, followed by DI water, acetone, and finally isopropanol. A 1.2 Molar solution of Methyl ammonium Iodide $MAPbI_3$ was prepared. Perovskite precursor, 507.1 mg of Lead iodide PbI_2 (TCI) was dissolved in 1 ml 1:4 dimethyl sulfoxide (DMSO): N, N-dimethylformamide (DMF) (both anhydrous, Sigma-Aldrich) [47]. The formed solution was stirred the whole night, spin-coated for 50 seconds at 3000 rpm, then annealed for 25 minutes at 105 °C. For **Anti solvent quenching** the mixed solution was spin-coated in two stages 1st at 3000rpm for 30 seconds 2nd at 4000rpm for 20 seconds while in between the chlorobenzene (Anti-solvent) was poured at 10 seconds of 2nd stage coating then annealed for 25 minutes at 105 °C. For **Gas annealed** the mixture was spin-coated at 3000rpm for 50 seconds and then annealed for 2 minutes at 105 °C. After that it was exposed to the vapors of methyl amine. Again it was annealed for 5 minutes.

5.2 Perovskite Solar Cell Fabrication

We have mainly focused on ($FTO/SnO_2/MAPbI_3/Spiro/Au$) architecture for the fabrication and its analysis since the same stack has been used for the simulations also. All the depositions have been carried out by spin coating. In the following sub-sections, the detailed method that has been implemented for the fabrication of solar cells has been discussed.

5.2.1 Substrate Cleaning

Before going to actual fabrication, the most important thing is substrate cleaning. Substrate cleaning is pivotal in achieving high-quality PSCs with improved performance and stability. The substrate should be free from any contaminants, such as dust, oils, grease, or residues, that

could interfere with the deposition and quality of subsequent layers. The level of substrate cleaning required can vary depending on the specific fabrication process and the cleanliness standards desired. Generally, a high level of cleanliness is recommended to minimize contamination and optimize the performance of perovskite solar cells. Now here we are going to use FTO as it belongs to the category of TCO (discussed in section 1.2.3)for device fabrication. The FTOs have been cut with the dimensions of $2cm \times 2cm$. These FTOs were first cleaned by the usual process of ultrasonic bath for 25 min each in deionized (DI) water with soap solution, DI water, acetone, and isopropanol, respectively. After the normal cleaning process, these substrates were dried with a **Nitrogen gun**. It provides a high-velocity stream of clean, dry nitrogen gas to remove particles, dust and other contaminants from the surface of a substrate. Nitrogen gas is also moisture-free and helps to dissipate static charges on the substrate surface, reducing the potential for re-attracting particles and improving overall cleanliness which makes it suitable for cleaning applications.

Figure 5.1: Photograph showing nitrogen gun typically used for substrate cleaning

while a nitrogen gun can be effective for removing loose particles and surface contaminants, it may not be sufficient for removing more stubborn or adherent contaminants. In such cases, additional cleaning methods, such as solvent cleaning or plasma cleaning are necessary. Therefore after drying it with nitrogen, we did the plasma cleaning of all the cut FTOs. The air plasma cleaning was done for 40 seconds. Then these substrates were properly put inside the desiccator in a vacuum before taking it to the

ETL coating.

Figure 5.2: photograph showing Microwave Plasma Cleaner used for substrate cleaning

5.2.2 FTO patterning :

Creating a pattern or defining specific areas in the FTO layer is crucial for subsequent steps in device processing. To define the preferred etching pattern, we utilize a protective mask of Kaptone tape, which is applied to a part of the FTO layer. The exposed FTO substrate then receives a coating of Zinc Powder mixed with a 4M HCl solution, and we allow the reaction to run its course. The metallic zinc engages in a reaction with HCl, resulting in the production of nascent hydrogen which is capable of etching TCOs (ITO/FTO). Following this reaction, the etched area of the substrate is then wiped clean with a cotton swab, applying firm pressure. The final step involves rinsing the area with DI water to ensure a clean surface for further processing.

5.2.3 Layers coating

To deposit the **ETL** commercially available Alfa Aeser SnO_2 having (15 % H_2O colloidal solution) was diluted in 1:4 proportion in DI and spin-coated at 3000rpm for 30 seconds. These substrates are annealed at 150°for 30 minutes. The coated SnO_2 was taken to the UV treatment for cleaning before transferring it to the glove box for perovskite deposition.

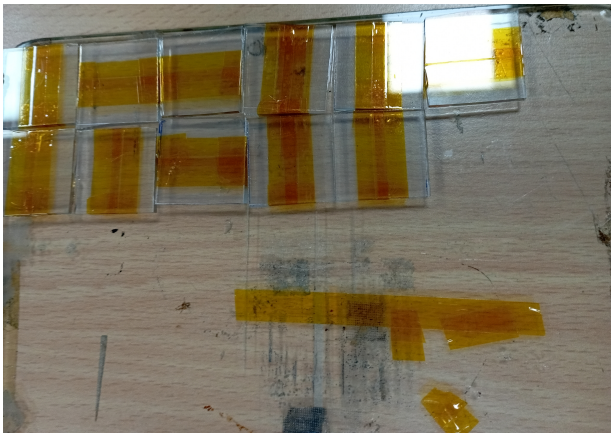

Figure 5.3: Photograph showing masking of all substrate using kaptone tape for etching FTO from unmasked region

UV light can break down organic contaminants on the substrate surface through photochemical reactions and therefore, improve the wettability of perovskite solution by reducing the contact angle [48].

Figure 5.4: Photograph showing UV- ozone cleaning setup used to clean any organic contaminants of all substrate using kaptone tape for etching FTO from unmasked region

Perovskite coating These were then coated with $MAPbI_3$ (1.2M) with the solution prepared in section 5.1.1 at 4000rpm for 50 seconds and annealed for 2 minutes at 105 °. These were then brought out of the glove box to do gas annealing (optimized above) with methyl amine (since it contains 50% water). After that, it was exposed to the vapors of methyl amine. Again it was annealed for 5 minutes inside the glovebox [49].

For **HTL coating** (spiro-OMeTAD) at a concentration of 86mL[1], in 1mL of chlorobenzene was prepared. This solution was doped with 4−tertbutyl-pyridine (TBP Sigma) and lithium bis(trifluoromethane sul-

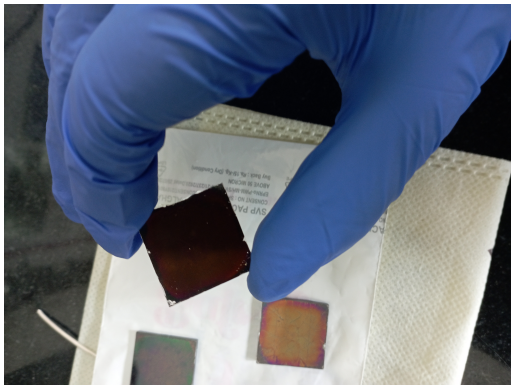

Figure 5.5: Deposited perovskite layer

fonyl) imide (LiTFSI Sigma) Here, 34 μL of TBP and 20 μL of LiTFSI (785 μL[1] in acetonitrile) were added per 1 mL of spiro-OMeTAD solution [49]. The resultant solution was dynamically spin-coated at 4000 rpm for 60 seconds. The films were then allowed to oxidize overnight inside a desiccator filled with dry oxygen. The next day the Gold **back contact** was thermally deposited in a thermal evaporation unit at 1A/second rate and 80 nm thickness.

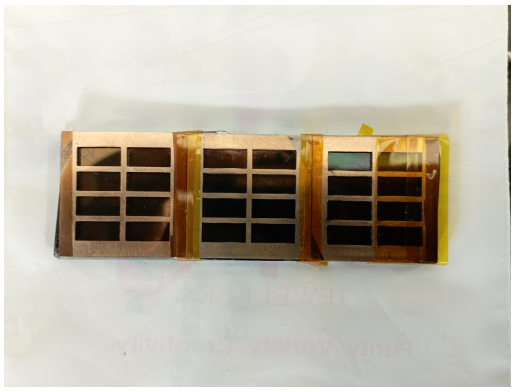

Figure 5.6: Masking for Gold Evaporation

This evaporation was performed through a conformal mask having eight pixels (cells) made up of stainless steel.

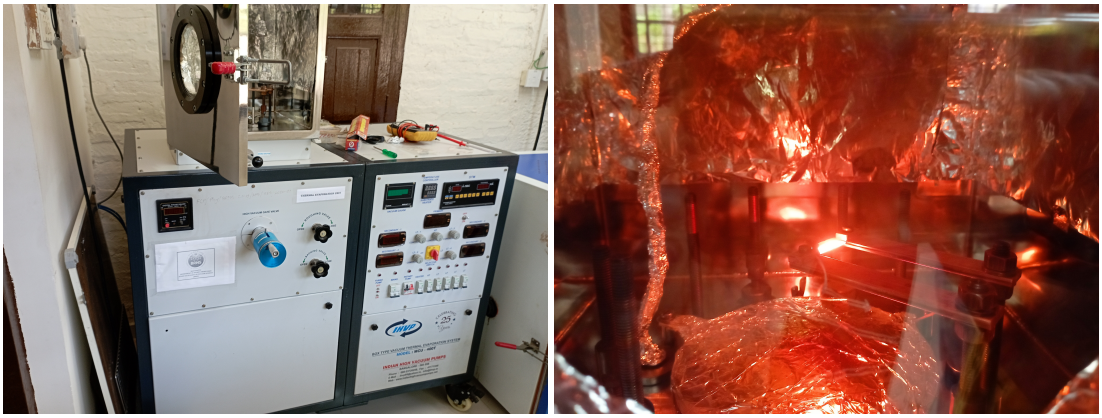

Figure 5.7: (A) Thermal Evaporation Unit. (B) Evaporating Gold on device

After deposition, these masks were peeled off from the films. Then we put it into the argon-filled glovebox. Here is the image of our fabricated solar cells.

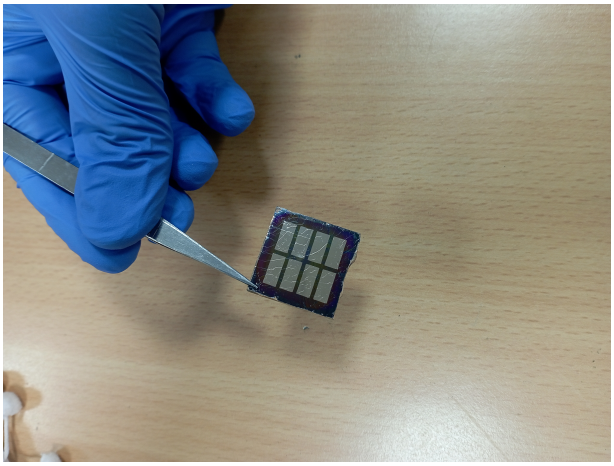

Figure 5.8: Photograph showing a final fabricated solar cell with Gold over top

Chapter 6

Results and Discussion

In this chapter, we are going to discuss the simulated results (TMM and DDM) as well as the experimental results. We will also establish a relation between both results.

6.1 Simulation Results

simulated results of perovskite solar cells can provide valuable insights into their optoelectronic properties, defects and traps, stability, and performance in solar cells, helping to guide the development of more efficient and stable devices. Also, these results are very important for certain commercial applications like Building integrated Photovoltaics and solar power plant.

6.1.1 TMM results

For simulating our perovskite solar cell, we are using the following materials (as discussed in the introduction part) and their respective thicknesses taken in accordance to have minimum parasitic absorption and maximum active layer absorption.

Type	Material	Thickness(nm)
Perovskite	$MAPbI_3$	600
HTL	Spiro	200
ETL	SnO_2	30
Substrate	ITO/FTO	110
Electrode	Au/Ag	100

Table 6.1: Table for Thickness of different layers in the Simulated PSC

E-Field Intensity in Device

The performance of a PSC is significantly influenced by the spatial variation of the electric field intensity (E-field) of the incident wave within the device. From Figure 6.1, it can be seen that the intensity of the electric field is maximum at the interface from which light is incident (for n-i-p it is the ITO-SnO_2-Perovskite interface) and attenuates rapidly as it progresses through other layers in the device stack. As a result, the interface experiences the highest levels of light absorption and electron-hole pair generation. This is mainly because of the high absorption coefficient of $MAPbI_3$ for visible light. However, one can observe that for the 400 nm wavelength, the attenuation with position (or thickness of perovskite layer) is faster than the 500 or 600 nm light. This is in accordance with the higher value of absorption coefficient of $MAPbI_3$ for blue wavelength than the green or red wavelengths. It also signifies that the blue wavelengths (380 – 450 nm) are almost completely absorbed near the ITO-SnO_2-Perovskite interface whereas the complete harvesting of the green and red part of the solar spectrum needs higher thickness of perovskite (due to its lower absorption coefficient than 400 nm). The E^2 profile with thickness hints at the possible charge-carrier generation rate profile which is discussed further in the subsequent section.

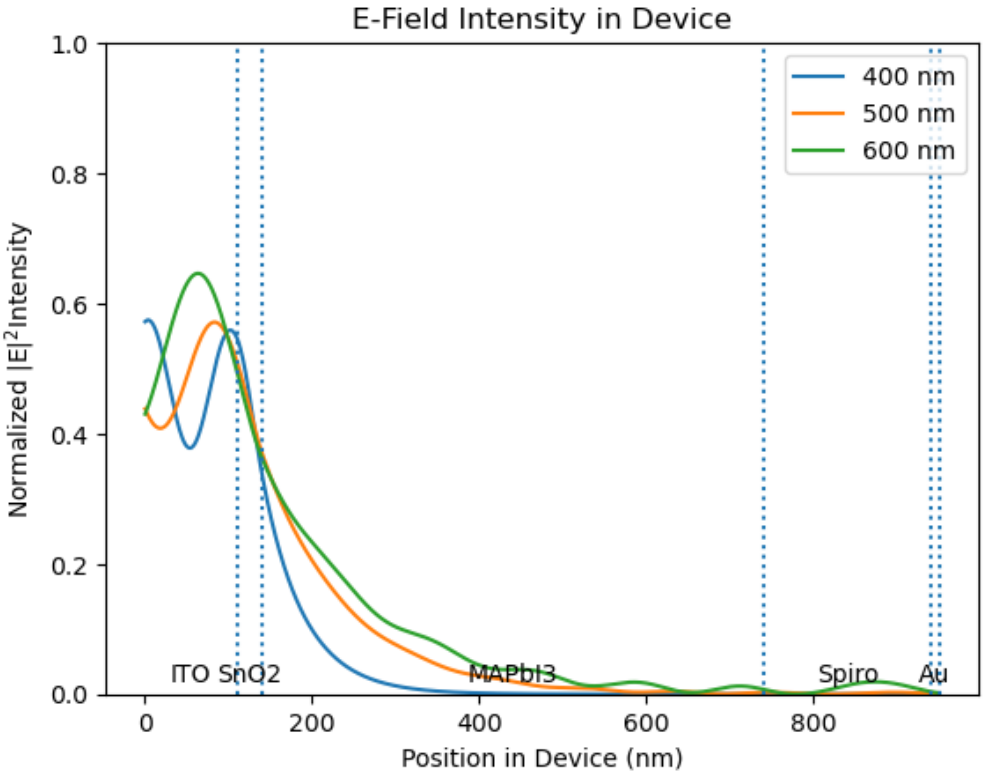

Figure 6.1: Simulated Plot of Electric field intensity as a function of position in the device for light of different incident

Light absorbed or reflected

The light being absorbed by the active layer largely affects the efficiency of the PSCs. Hence the optimization of the thickness of active and other layers are crucial to have the maximum absorption inside its active layer.

it can be seen that for light incident from the ITO-SnO_2 side in n-i-p architecture, the ITO, SnO_2, and Spiro-MeOTAD show minimal absorption in the visible range i.e. 400 – 800nm. This is particularly beneficial for device performance as any absorption in these layers would lead to parasitic losses. SnO_2 being the high band gap (3.3 eV) n-type semiconductor and low thickness (30 nm) used in PSC stack leads to minimal parasitic losses. On the other hand, properly oxidized Spiro-MeOTAD can have absorption onset at 420-450 nm, however, because it is placed at the other end of the device stack, most of the 400 – 450 nm light is completely absorbed in the perovskite and therefore, the question of parasitic absorbance in Spiro-

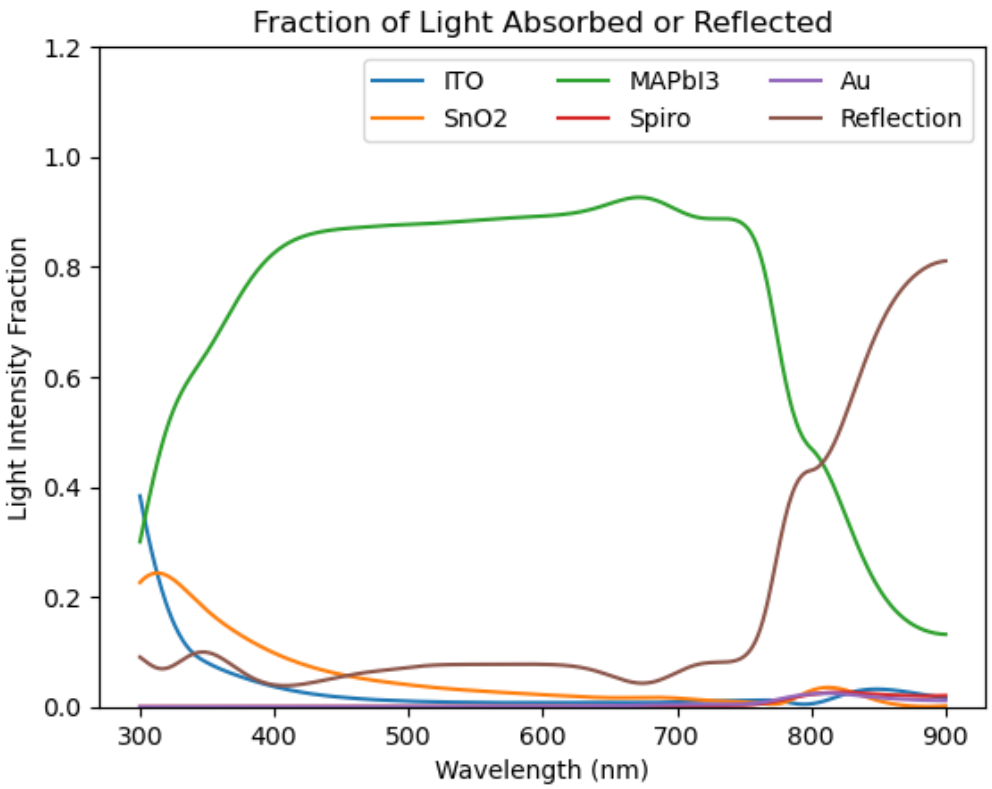

Figure 6.2: Simulated light absorbed and reflected as function of wavelength at each layer in the device stack

MeOTAD does not arise in n-i-p architecture devices. However, as shown later in the thesis, the use of Spiro-MEOTAD in p-i-n architecture where the light first encounters the Spiro-MeOTAD layer, leads to substantial parasitic absorbance. Importantly, the perovskite layer harvests the full visible region of the electromagnetic spectrum as shown by the green curve in figure 6.2. This is mainly due to the low bandgap of $MAPbI_3$ (1.54 -1.57 eV) which leads to an absorption onset at 800 nm. The extension of absorbance beyond 800 nm in the case of $MAPbI_3$ indicates the possible presence of tails states. This could also be possibly due to optical artifacts that may be present in the optical absorption experimental data used for the simulation.

Exciton Generation rate

The generation rate in a perovskite solar cell refers to the rate at which electron-hole pairs (excitons) are generated within the perovskite

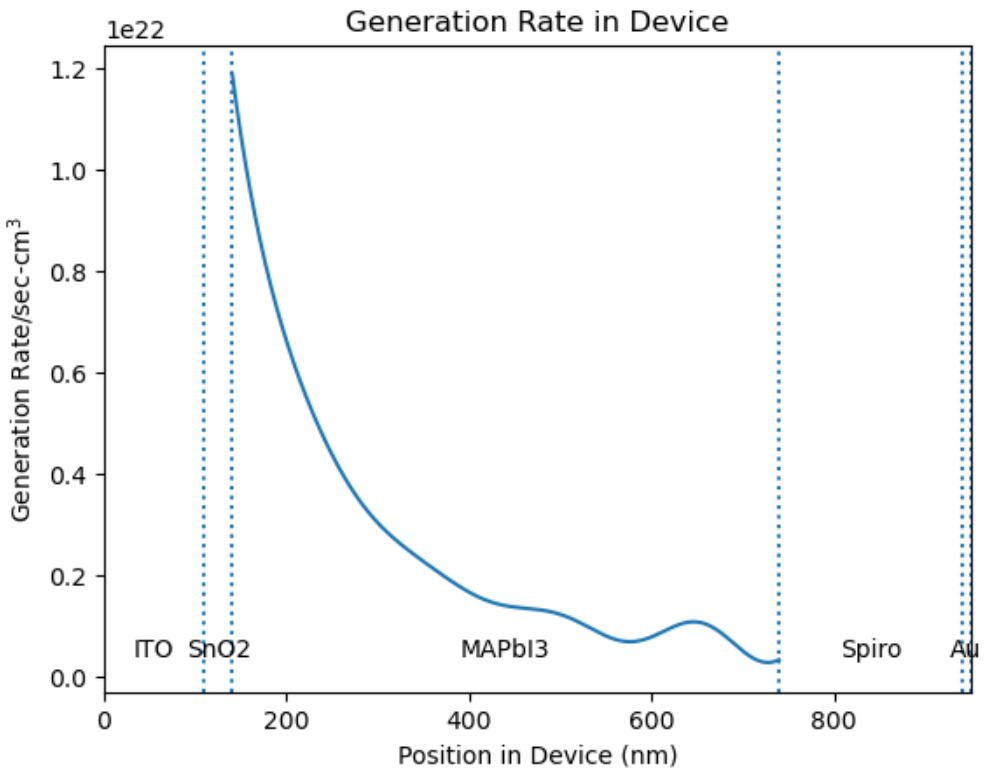

Figure 6.3: Simulated Exciton Generation Rate at each layer in the device stack

absorber layer as a result of absorbing photons from incident light. The number of carriers generated per unit time per unit volume at different positions in the device is plotted in Fig (6.3). It can be seen in the graph that most of the electron-hole pairs have been generated at this interface of SnO_2 and $MAPbI_3$ predominantly then it subsequently decreases according to the Beer-Lambert law. Such distribution is key to the diffusion of charge carriers within the device. The electrons generated are filtered by the ETL (SnO_2) which leads to a high concentration of holes at this interface over a certain amount of time. This leads to the concentration gradient of holes from the SnO_2-$MAPbI_3$ interface to the Spiro-$MAPbI_3$ interface creating a diffusion of holes towards the top contact. In summary, the concentration gradient of charge carriers along the thickness of the device combined with the electron and hole filtering layers leads to the concentration gradient and hence diffusion of electrons and holes in opposite directions. Yet there is a lump around 700nm due to thin internal interference.

Generation rate dependence on wavelength

The generation rate of a perovskite solar cell is a cumulative indicator of how the light is harvested within the device stack as a function of wavelength. Indeed, it depends on various parameters considered within TMM modeling including incident solar flux, absorbance/transmittance, reflectance, refractive index, and thickness of each layer. Therefore, the highest value of generation rate is for the wavelengths highest for wavelengths which is above the band gap of the perovskite active layer but which are also not parasitically absorbed by the transport layers. For instance, the wavelengths below 400 nm are predominantly absorbed by SnO_2/ITO/Glass these despite having energy higher than bandgap, do not result in the highest generation rate.

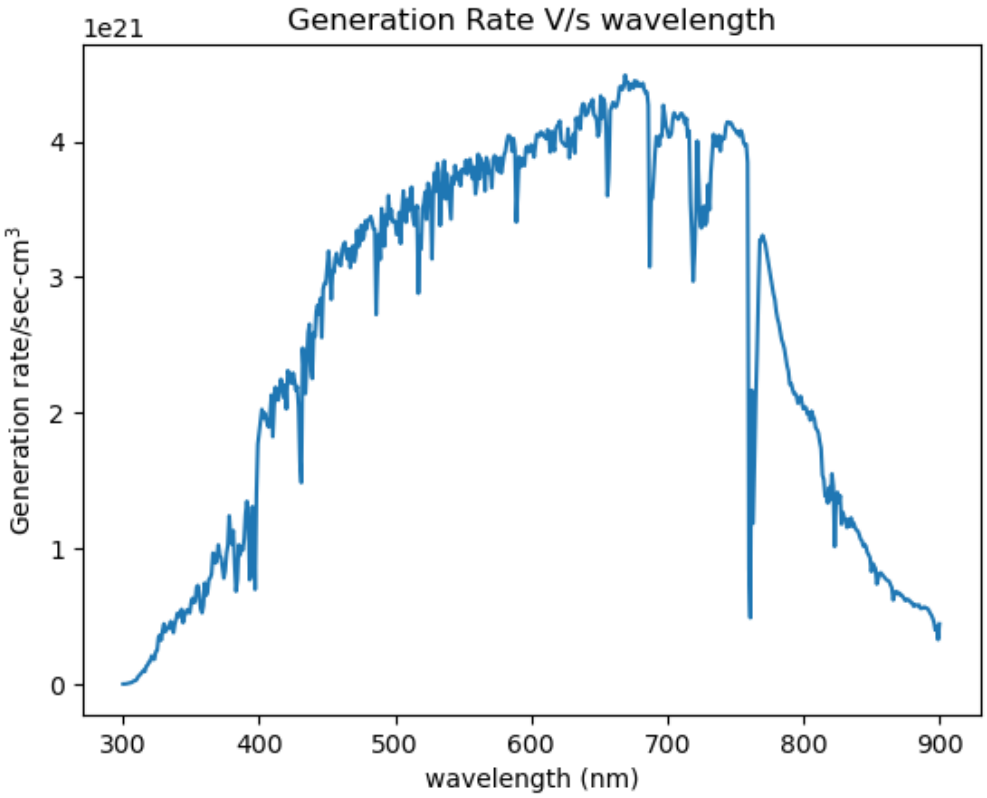

Figure 6.4: Simulated carrier generation rate as a function of wavelength in solar spectra.

Short Circuit Current Density (J_sc)

The highest J_sc achieved by this configuration is 25mA/cm^2. Simulated Jsc = 24.89 mA/cm^2

External quantum Efficiency

We calculated the External Quantum Efficiency (EQE) of this cell using equation 3.19 and hence obtained the 'idealized integrated Jsc' using equation 3.21. We found that the n-i-p device stack studied in this project is capable of delivering 90% EQE at 670nm with reasonably high values between 400 to 750 nm. Understandably, the EQE value falls rapidly near the band-edge of the perovskite active layer and also at wavelengths below 350 nm. The integrated Jsc yields a value of 24.89 mA/cm^2 for this stack.

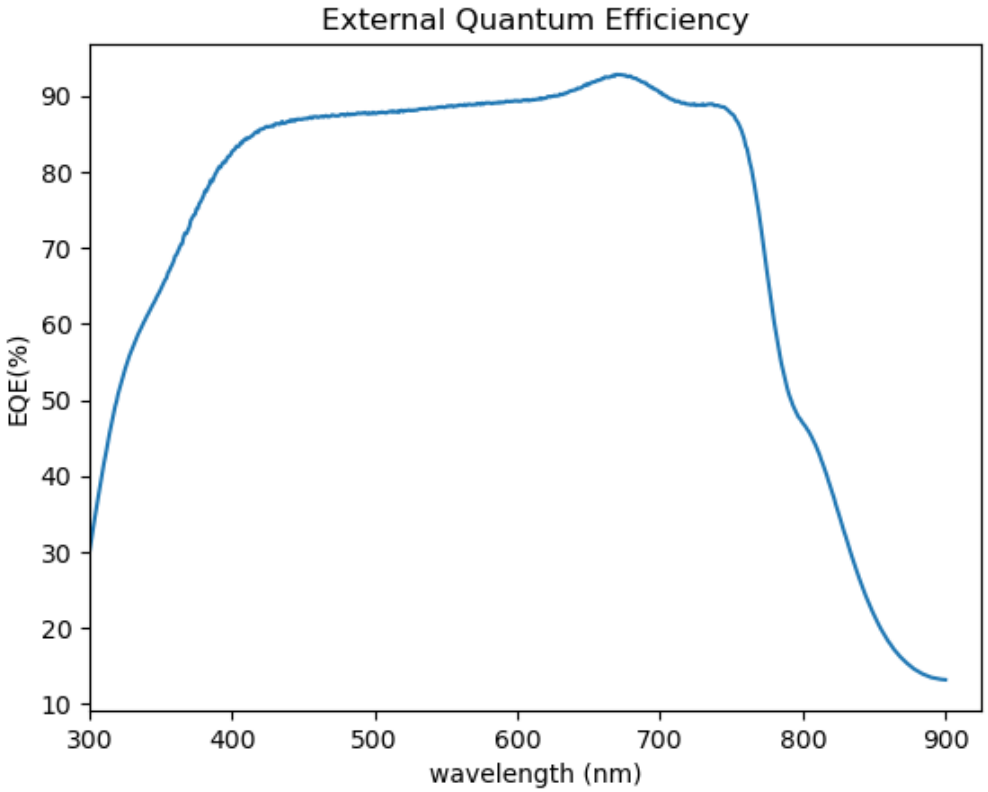

Figure 6.5: Simulated External Quantum Efficiency

Fractional EQE comparison of NIP vs PIN configuration

To demonstrate how parasitic absorbance in transport layers can dramatically affect light harvesting and hence EQE, we decided to simulate n-

i-p and p-i-n architectures with the same set of transport layers. Therefore, as shown in Figure 6.6, for n-i-p architecture, the SnO2 layer was deposited on the Glass/ITO contact followed by perovskite and Spiro-MeOTAD layer. Whereas, for p-i-n architecture, the Spiro-MeOTAD was deposited first on Glass/ITO followed by perovskite and SnO2.

It can be seen that in comparison with the n-i-p configuration, the p-i-n architecture the EQE dramatically reduces within the wavelength region 300 – 400 nm. This is because of the high absorbance of Spiro-MeOTAD within this wavelength region because of which the light of these wavelengths is not able to reach the active perovskite layer leading to parasitic losses. Whereas SnO2 is a high bandgap semiconductor (Eg 3.3 eV) and therefore, it does not absorb in this region leading to the transmittance of wavelengths between 300 – 400 nm to the active perovskite layer. This has a direct impact on the integrated Jsc with 24.11 mA/cm^2 for n-i-p vs 23.01 mA/cm^2 for p-i-n. This simulation result shows that the optical properties of transport layers (ETL/HTL) also play a very crucial role in light harvesting of a perovskite solar cell stack and minimizing the parasitic losses in the transport layer is one of the key objectives in device optimization. This result also highlights the reason for using ultrathin transport layers in p-i-n architecture PSCs so that the parasitic losses can be minimized.

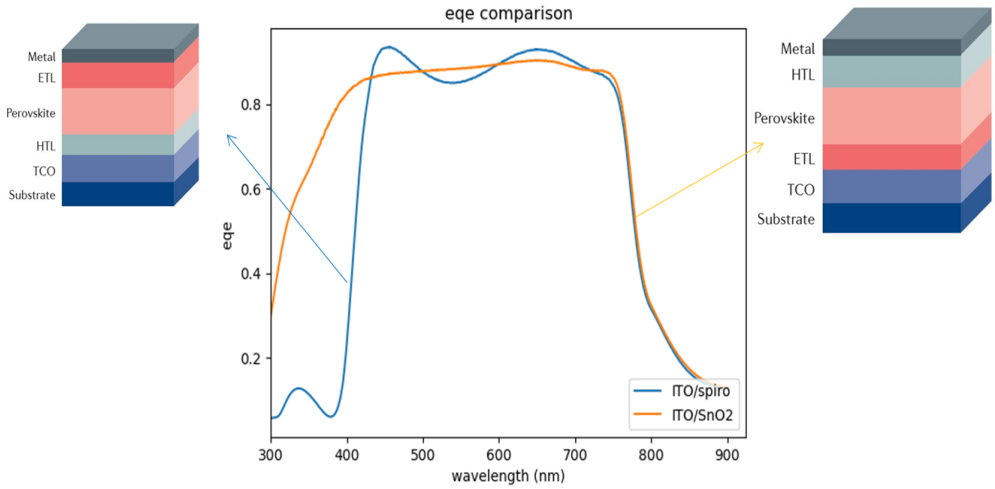

Figure 6.6: Simulated External Quantum Efficiency for NIP and PIN Configuration

EQE of PIN is higher than that of PIN configuration in the region of 300-400 nm that is because of the parasitic absorption of spiro in this region evident from Fig 4.2

EQE of Novel architectures

In the previous sections, we discussed mainly the TMM modeling of conventional architecture 'opaque' solar cells. However, the TMM modeling is particularly illuminating when used to understand light management within semi-transparent PSCs. These configurations are quite popular for Building Integrated Photovoltaics and tandem solar cells. In semitransparent PSC both the top and bottom electrodes are transparent conducting oxides viz. ITO. For our simulation, we assumed the conventional n-i-p architecture with SnO_2 and Spiro-MEOTAD as transport layers. We assumed the illumination from the top side (i.e. Spiro-ITO top interface side). Clearly, the parasitic absorbance from Spiro-MEOTAD limits the EQE in 300 – 400 nm region. Now some light is additionally lost due to both the top and bottom electrodes being ITO. This is more evident when the EQE of the device stack is simulated with a silver back reflector as shown in Figure 6.7 (b). It can be clearly seen that the presence of back reflector results in higher EQE particularly in long wavelength regions (750 – 800 nm).

This result particularly also indicates the usefulness of metal electrodes in conventional opaque perovskite solar cells. In the conventional architecture PSCs, the complete absorption of the near band-edge wavelengths rather needs active layer thicknesses greater than 1000 nm but processing such thick films is challenging and also the transport is limited by the diffusion length which is usually less than 200 nm. In such a scenario, the metal electrodes helps reflect the unabsorbed light back into the device stack to increase its path length resulting in a boost in EQE near the band edge. Since we already have a lot of discussion about the TMM simulated results of conventional architectures of PSCs. Now let's take a look at some of the Novel architectures like semi-transparent and Opaque(shown in fig 4.7).

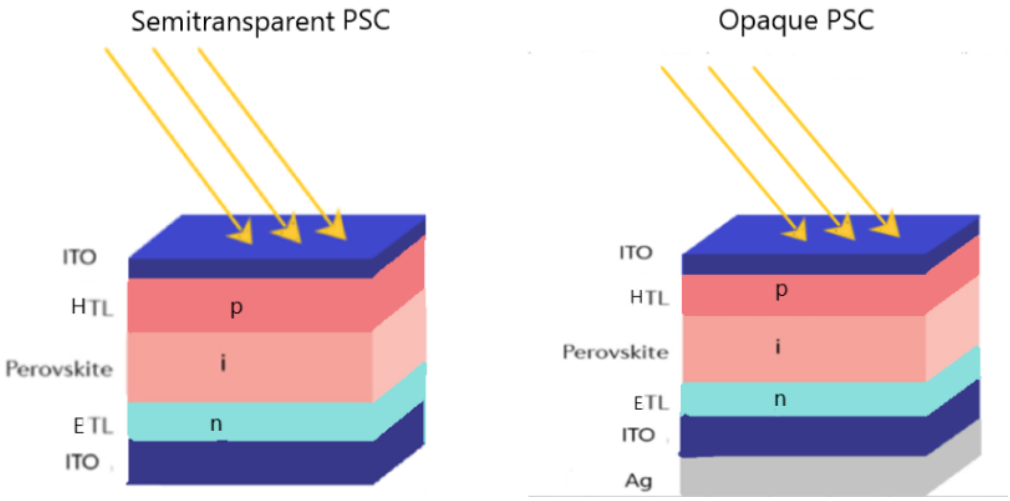

Figure 6.7: Shematic showing architectural differences in Semitransparent and opaque PSCs

These configurations are quite popular for Building Integrated Photovoltaics and solar power plants. In semitransparent PSC ITO itself is the top electrode while Opaque PSC has a reflector made of silver (Ag). This increases the path length of the light hence we are getting extended EQE. The materials used for this simulation are the same used for the above TMM simulation (FTO/SnO_2/$MAPbI_3$/Spiro/Au).

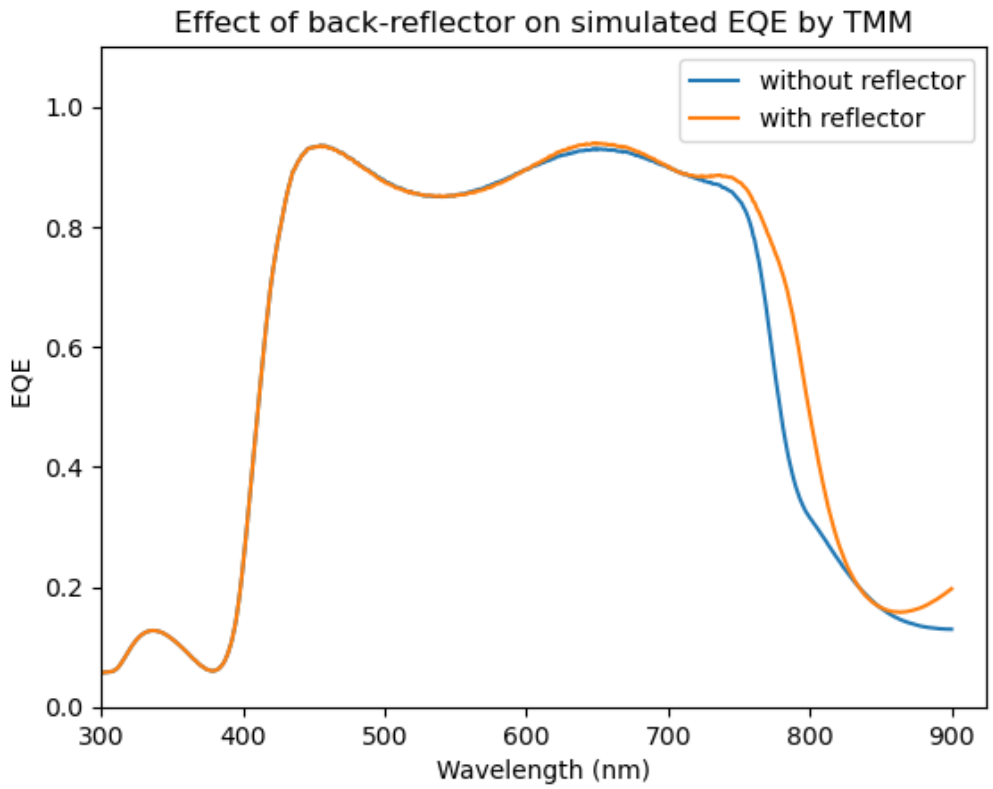

Figure 6.8: Effect of the back reflector on simulated EQE.

6.1.2 Drift Diffusion Model results

Thickness optimization

In our study, we utilized the Drift-Diffusion model to sequentially optimize the thickness of each layer in our perovskite solar cell stack, starting with the perovskite layer and followed by the Electron Transport Layer (ETL) and the Hole Transport Layer (HTL). After each optimization, we recorded the maximum efficiency achieved.

The thickness of the absorber layer, composed of ($MAPbI_3$), was altered within a range of 100 nm to 1200 nm. Following this, the thickness of the ETL, which consisted of tin dioxide (SnO_2), was varied within a span of 20 nm to 200 nm. During this process, the thicknesses of all other layers were held constant. Subsequently, the thickness that resulted in the highest efficiency was recorded.

A similar procedure was adopted for the HTL, where the thickness

was varied from 50 nm to 500 nm. The aim of these adjustments was to find an optimal balance that would maximize the efficiency of our perovskite solar cell while keeping in mind the limitations and requirements of each individual layer.

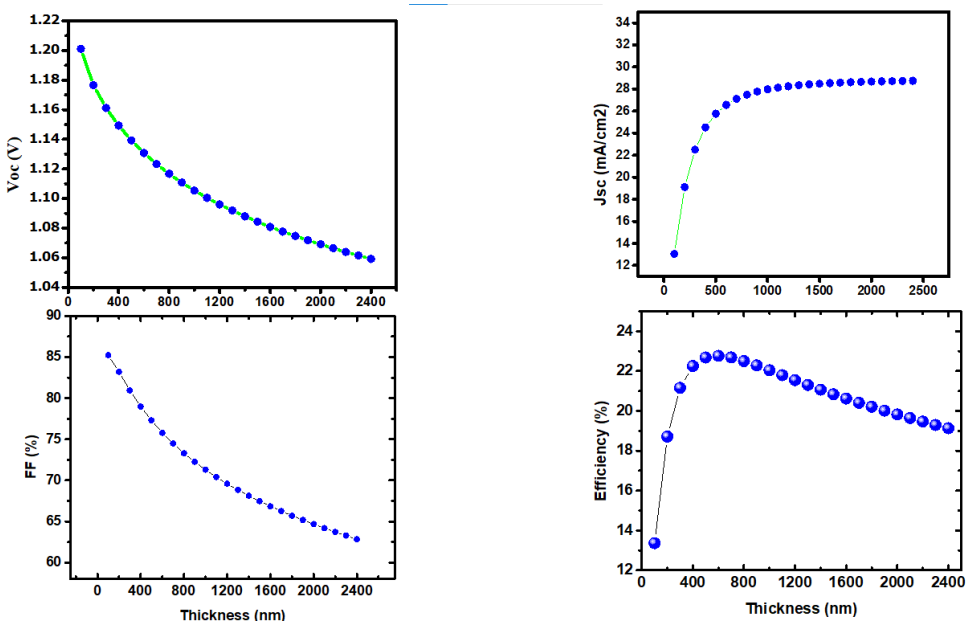

Figure 6.9: Influence of absorber thickness on PV performance parametrs of PSCs

The active layer in a perovskite solar cell, plays a critical role in power conversion efficiency (PCE). Optimal layer thickness is of utmost importance: a layer thinner than the optimal thickness can result in inadequate light absorption, while an excessively thick layer may lead to an increase in charge recombination. Both scenarios adversely affect the fill factor (FF) and the open-circuit voltage (Voc), hence reducing the overall cell efficiency. Our simulation results demonstrate a clear relationship between the thickness of the active layer and the PCE. An increase in layer thickness up to 800 nm resulted in an enhancement of the short-circuit current (Jsc), but beyond this point, Jsc plateaued.

Conversely, Voc and FF indicated a decline with increased thickness, suggesting a rise in recombination events and increased resistance, respectively. Interestingly, our data showed a significant surge in PCE with an initial increase in thickness, reaching a peak at approximately 750 nm. Beyond this thickness, however, the PCE started to decline, mirroring the

observed reduction in Voc and FF. Given these findings, we established 750 nm as the optimal thickness for the methylammonium lead iodide ($MAPbI_3$) perovskite layer. This optimization is dependent on the specific composition of the stack layers used in our study and may vary under different conditions. We assert that this optimized thickness ensures a balanced trade-off between light absorption and charge recombination, thus maximizing the cell's power conversion efficiency.

ETL Thickness optimization

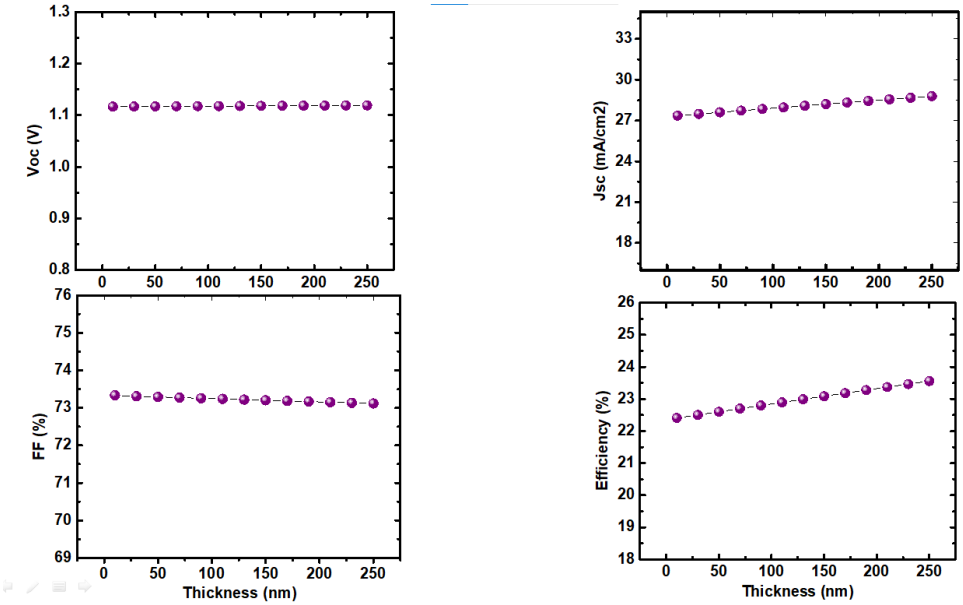

Figure 6.10: Influence of ETL thicknesson PV performance parametrs of PSCs

The thickness optimization of the Hole Transport Layer (HTL) and Electron Transport Layer (ETL) in a perovskite solar cell is equally crucial for achieving efficient charge transport, minimizing recombination losses and parasitic absorption losses and maximizing device performance. For an increase in ETL and HTL thickness there has been a negligible change in all the photovoltaic parameters this shows that SCAPS 1D doesn't take into account the internal resistance change of the device due to the increasing thickness of HTL and ETL respectively. It also doesn't takes into account of increase in parasitic absorption due to the increasing thicknesses of both layers. Therefore, concluding the exactly optimized ETL and HTL thicknesses could not be possible using SCAPS-1D simulation alone. There

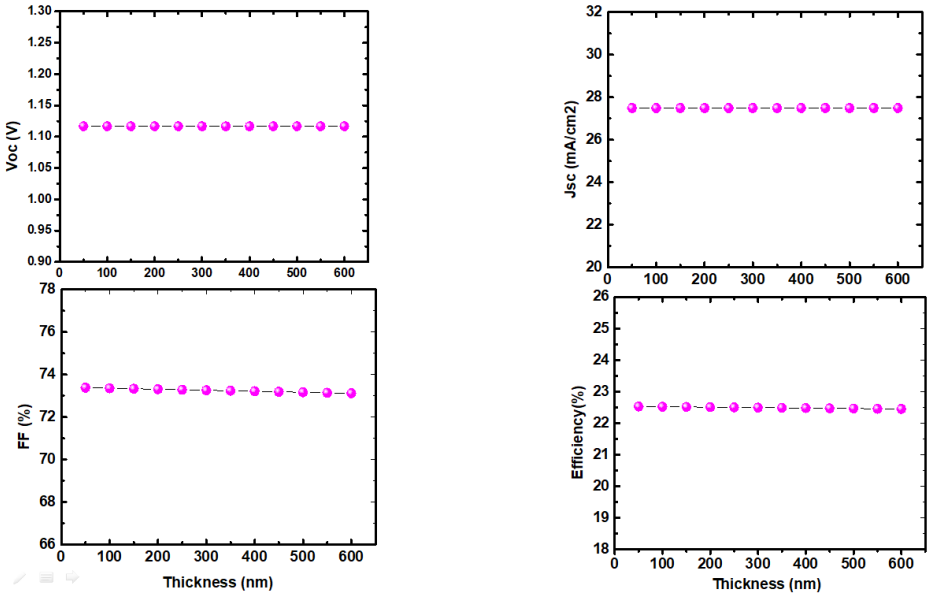

Figure 6.11: Influence of HTL thickness on PV performance parametrs of PSCs

is a need to incorporate the optical modeling along with material thickness dependence of series and shun resistance within SCAPS-1D.

Absorber Defect Density Optimization

The defect density in the absorber layer of a perovskite solar cell refers to the concentration of defects or imperfections present within the perovskite material. Defects can arise from various sources, such as impurities, crystal lattice defects including vacancies and interstitials grain boundaries, or interface defects. The higher defect density of the perovskite material leads to greater recombinations as suggested in eq (4.8). Therefore, It leads to a monotonic decrease majorly in Voc and FF. However, for defect densities below 1016 cm^{-3} the Jsc had little effect but decreased rapidly for higher defect densities.. The experimentally reported defect density of $MAPbI_3$ (absorber layer) is 10^{15} to 10^{16} cm^{-3}[50]. Hence to get reasonable agreement between the experiment and simulation the intrinsic value of defects was chosen to 10^{15} cm^3.

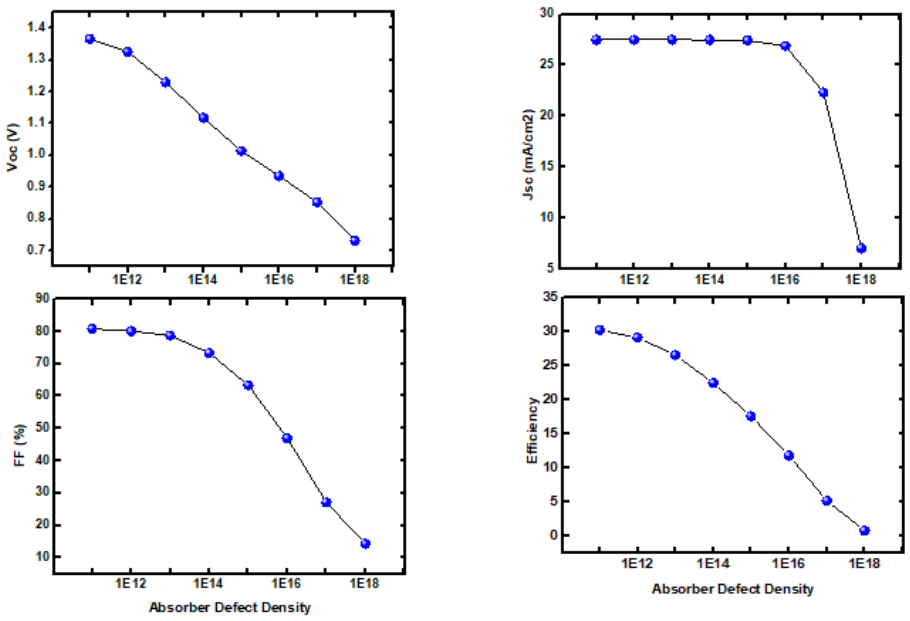

Figure 6.12: Influence of Absorber defect density on PV performance parametrs of PSCs

Resistances

Series Resistance

Series resistance is the resistance that exists within the electrical path of a solar cell, including the resistance of the materials, contacts, and interconnects. The efficiency is maximum for zero resistance which is not possible practically. The device performance decreases with an increase in series resistance. Its increase affects the maximum power point voltage.

$$Vmpp = V_{oc} - (Isc \times Rs) \tag{6.1}$$

As a result, it affects the Fill Factor and Efficiency subsequently. The optimized series resistance lies in between $2 - 6\ \Omega\ \text{cm}^2$ for better cell performance.

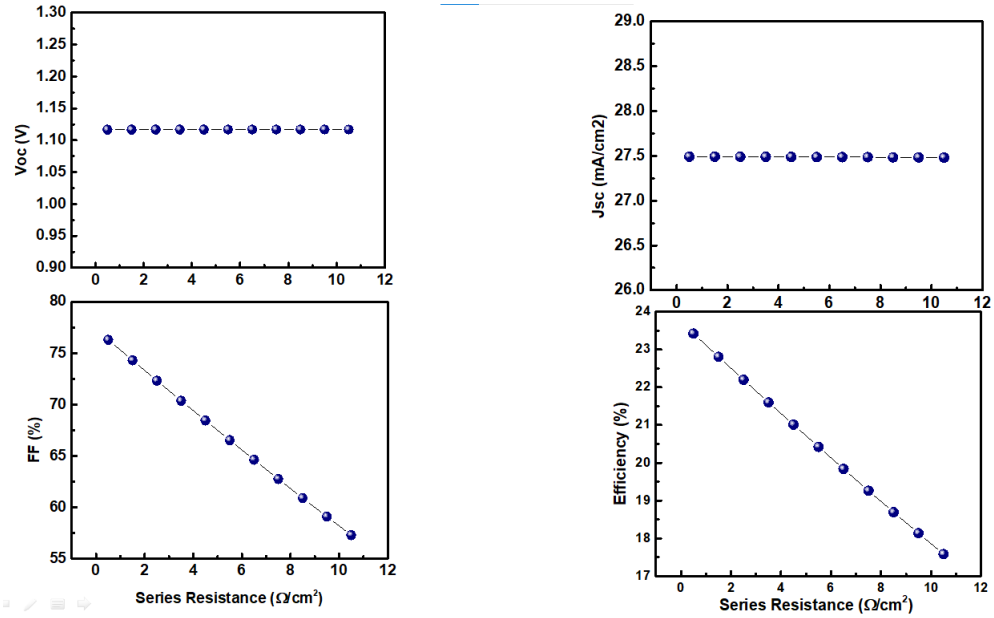

Figure 6.13: Influence of Series resistance on PV performance parametrs of PSCs

Shunt Resistance Shunt resistance represents the resistance that counteracts the 'leakage' of current in a solar cell, which occurs from one side of the cell to the other. This leakage can be attributed to imperfections within the cell. It is also often referred to as parallel resistance or bypass diode resistance, significantly influencing various critical photovoltaic (PV) parameters. These include current-voltage (I-V) characteristics, the maximum power point (MPP), and other key photovoltaic performance indicators.

Theoretically, the optimal performance of a perovskite solar cell (PSC) can be achieved with an infinitely high shunt resistance. However, in real-world conditions, achieving such high resistance is implausible due to the presence of material defects such as pinholes and cracks. These imperfections can facilitate current leakage, thereby reducing the device's shunt resistance and, consequently, its overall performance. Our findings suggest that all the photovoltaic parameters improve as the shunt resistance increases, reaching a plateau of around 10^5 Ω cm^2. This value appears to be the optimal figure that yields the best performance of the cell. In conclusion, optimizing shunt resistance is pivotal for maximizing the performance and efficiency of a perovskite solar cell.

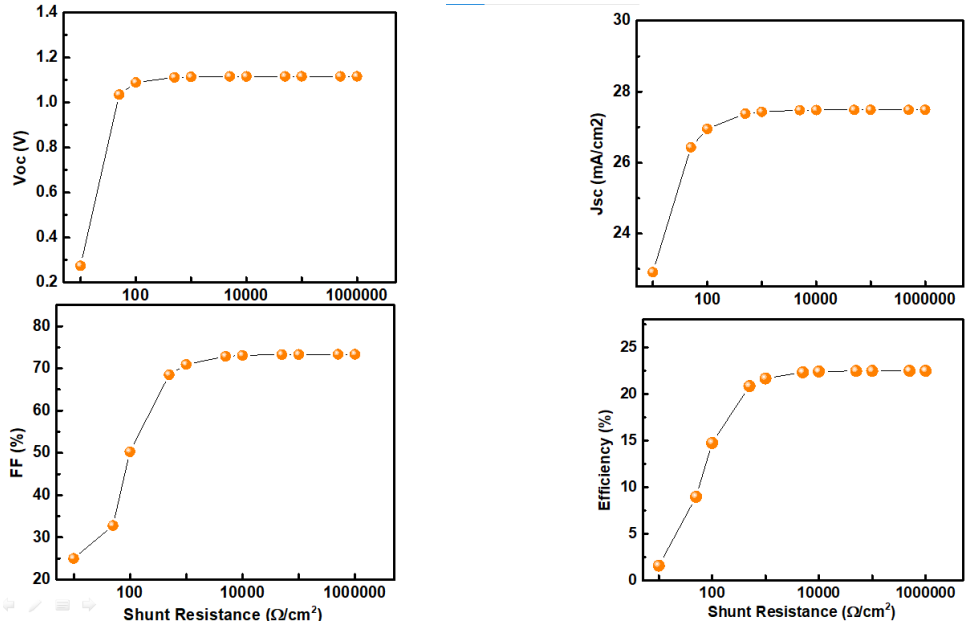

Figure 6.14: Influence of Shunt resistance on PV performance parameters of PSCs

Operating Temperature

Elevated operating temperatures have considerable impact on the optoelectronic characteristics of perovskite solar cells (PSCs), often leading to a decline in their performance parameters due to thermally-induced stress. Specifically, as the temperature rises, there is a notable decrease in Voc. This is primarily due to the increase in reverse saturation current, as described by equation (4.13), which in turn results in a reduction in FF and overall cell efficiency.

Notwithstanding these observations, it's important to note that the standard operating temperature for most solar cells, including PSCs, is approximately 300 Kelvin. At this temperature, the cells can maintain an equilibrium between performance and longevity. Consequently, understanding and managing the effects of temperature on PSCs are crucial for optimizing their operational efficiency and lifespan.

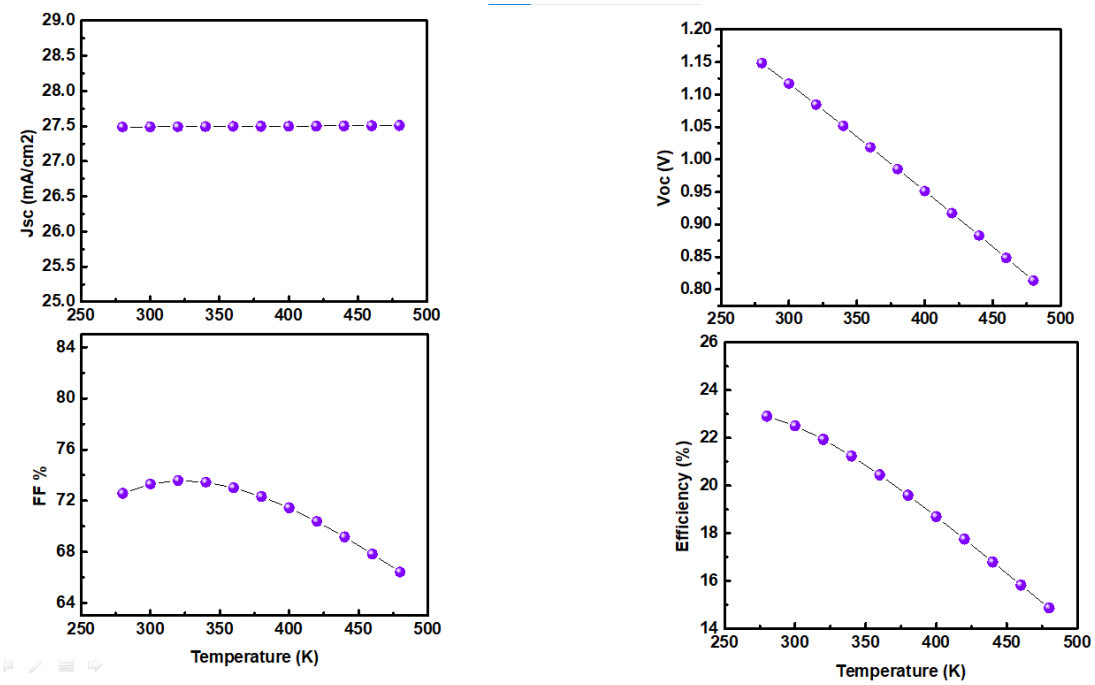

Figure 6.15: Influence of Temperature on PV performance parametrs of PSCs

Back Contact Work Function

The work function of back contact of PSCs also plays a significant role in affecting their performance. The work function of the top electrode should be compatible with the adjacent layers to ensure efficient charge extraction. It is important for achieving a suitable energy level alignment and facilitating charge carrier extraction at the interface between the top electrode and the perovskite layer. It can be seen in Fig (6.16) that Au, Ni, and Pt are good metals for achieving maximum efficiency but Ni is quite reactive to moisture and oxygen as a result it can't be used as a back contact for practical applications. While Pt and Au have better stability in the harsh environment.

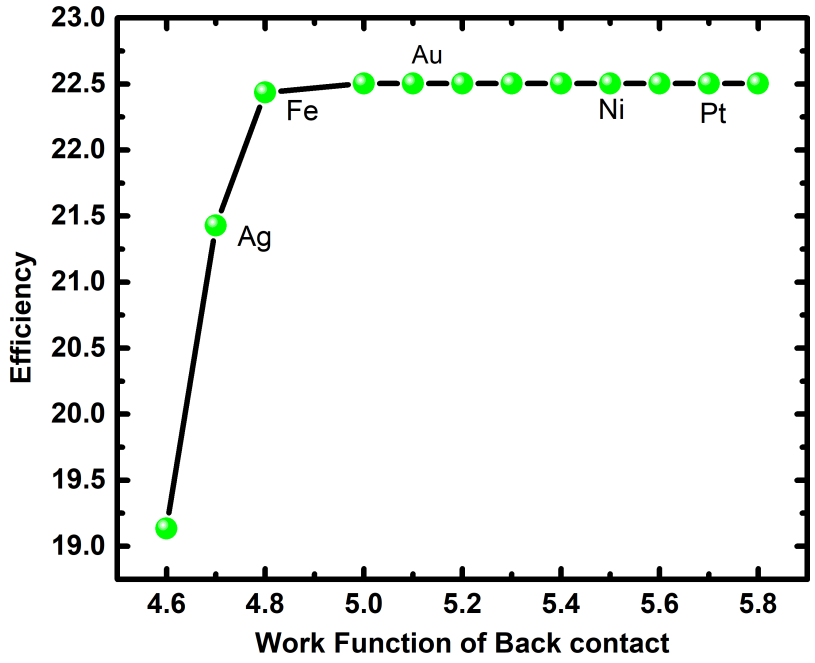

Figure 6.16: Influence of Back contact on Efficiency of PSCs

Extrinsic and intrinsic perovskite

During my work on the DDM simulations, I was also curious to investigate the effect of intrinsic and extrinsic (n and p type) behavior of $MAPbI_3$ on the efficiency of PSCs. In fig (6.17) donor density is fixed at 1×10^{11} as reported et. al Julie Euvrard [51] [52] [53] and the acceptor density is varied from 10^8 cm^{-3} to 10^{20} cm^{-3} we can see the PCE is nearly constant for intrinsic and n-type perovskite. But beyond a doping density of 10^{15} cm^{-3} an increase in PCE is observed. This implied that if we are able to dope the halide perovskites extrinsically to reasonable densities(10^{15}-10^{15} cm^{-3}) then the PCE of $MAPbI_3$-based solar cells could be boosted to 26 – 27%. Indeed such extrinsic doping is not easy considering $MAPbI_3$ to be a compound semiconductor with bands mainly composed by hybridization of Pb and I levels. Replacing I with other halides (F, Cl, Br) rather increases the bandgap. Also, vacancy defects in halide perovskites do not lead to self doping of perovskite (unlike metal oxides with oxygen vacancies).

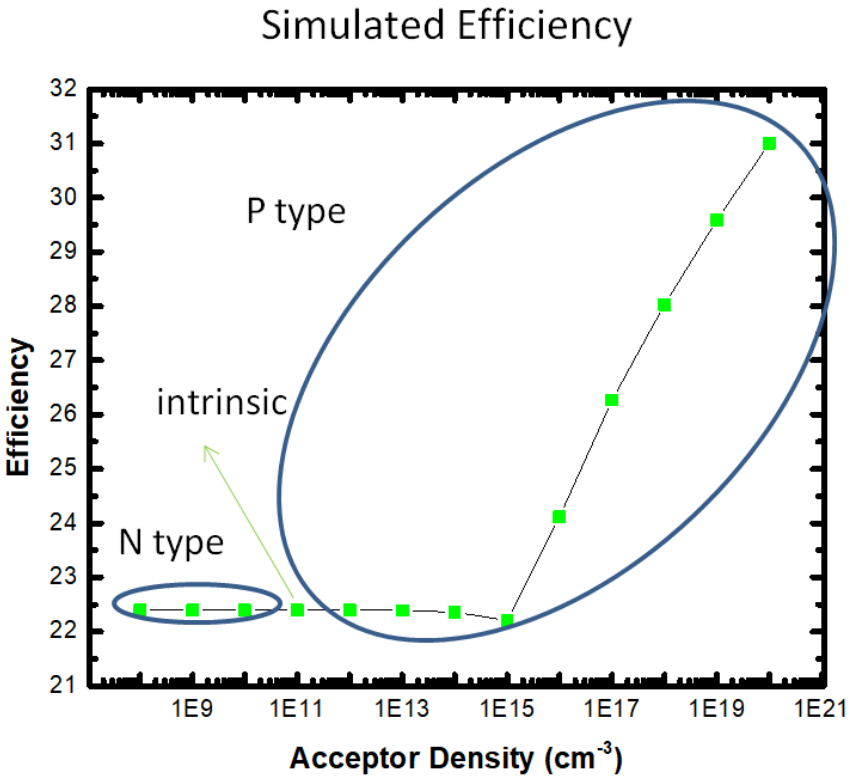

Figure 6.17: Influence of type of doping (extrinsic and intrinsic) nature and doping type of active perovskite layer on efficiency of PSCs

6.2 Experimental results

In this section, I will be describing the results that I got from perovskite ($MAPbI_3$) synthesis and PSCs device fabrication.

6.2.1 $MAPbI_3$ results

$MAPbI_3$ thin films were synthesized using normal spin coating, Anti-solvent quenching, and gas annealing methods. Their structural and morphological studies were analyzed and optimized for boosting the overall device performance.

X-ray diffraction

X-ray diffraction (XRD) is a frequently employed method for identifying the crystal structure and assessing the phase purity of perovskite films. It provides essential details about the crystalline phases, crystallographic orientation, lattice dimensions, and any impurities present. The operation of XRD analysis necessitates an X-ray diffractometer, usually composed of an X-ray source, a sample holder, and a detector. The X-ray source generates X-rays, typically of the copper K wavelength (= 1.5406 °A) or other energies appropriate for perovskite materials. The X-rays diffracted from the sample are recorded by the detector, leading to a diffraction pattern that is subsequently analyzed. The observed diffraction patterns span a 2 range from 10 °to 90 °C, gathered in increments of 0.026 °over a duration of 1.18 seconds per step. The chosen step size effectively discloses information related to each peak.

It can be seen in the XRD plot Fig 6.18 that raw and anti-solvent films don't have any preferential orientation while for Gas annealed $MAPbI_3$ orientational growth has been seen along (110), (220), and (330). This occurs because methylamine gas temporarily converts the $MAPbI_3$ phase into a liquid-like phase (via MA intercalation). Upon removal of excess MA pressure, the film first forms nucleation which probably has a preferred orientation along 110 which results in further growth along this direction resulting in highly oriented $MAPbI_3$ film.

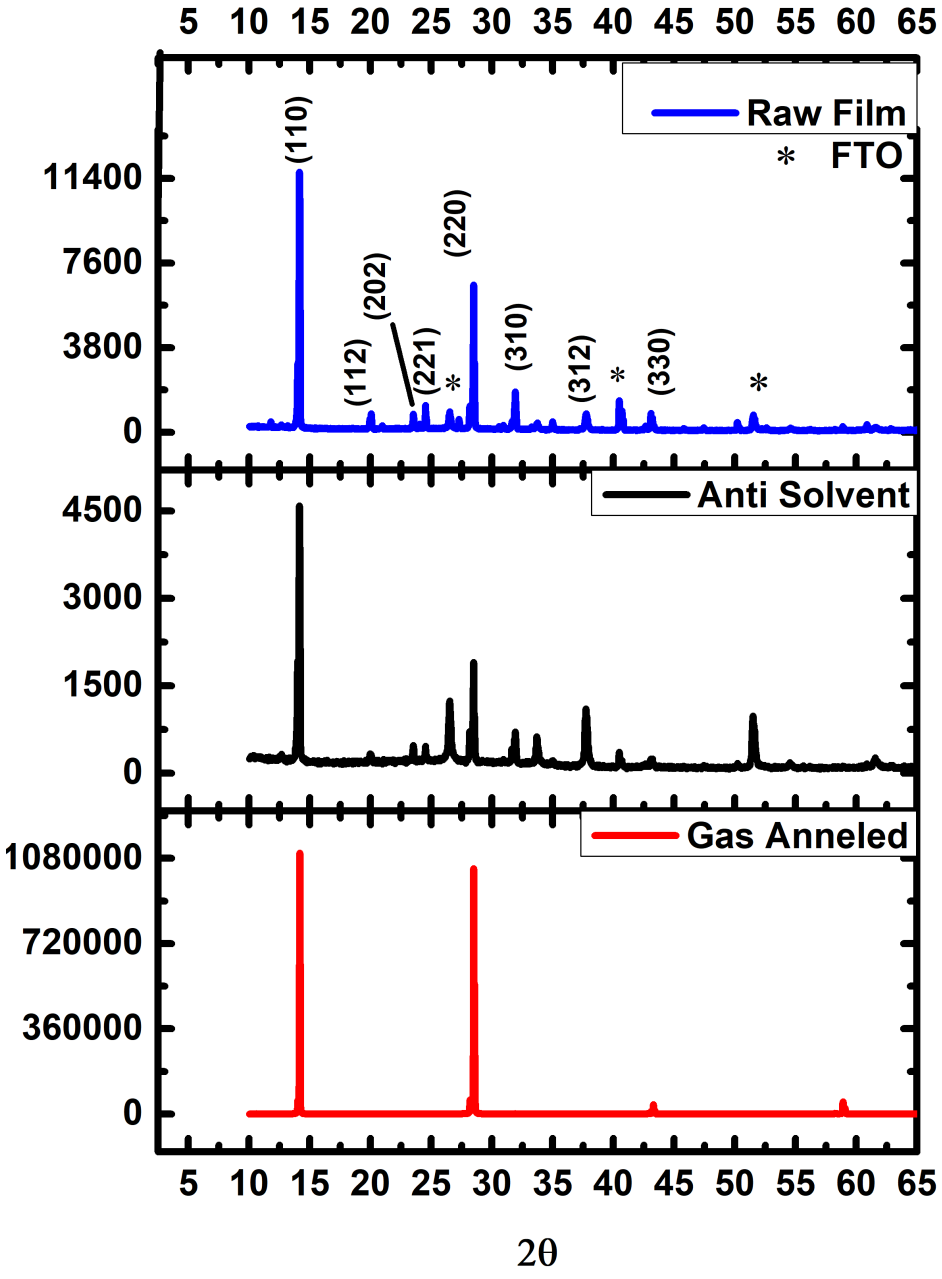

Figure 6.18: XRD plots of $MAPbI_3$ deposited by different methods

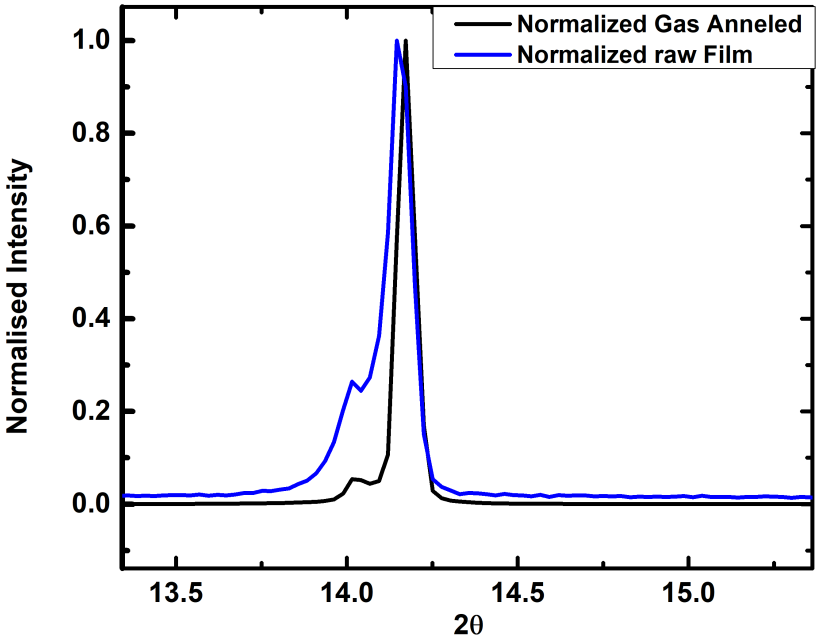

Figure 6.19: Normalized Intensity graph of (110) XRD peak of Gas annealed and raw film of $MAPbI_3$

Fig 6.19 shows the normalized intensity peak v/s 2θ for gas annealed and raw film. The FWHM of the gas-annealed film is lesser than the raw film which indicates its more crystallite size according to the debye- sheerer formula.

Fig 6.20 shows the logarithmic intensity plot of XRD results of both films indicating that Gas annealed $MAPbI_3$ has three orders higher intensity than its raw film implying preferential growth along the (110) axis.

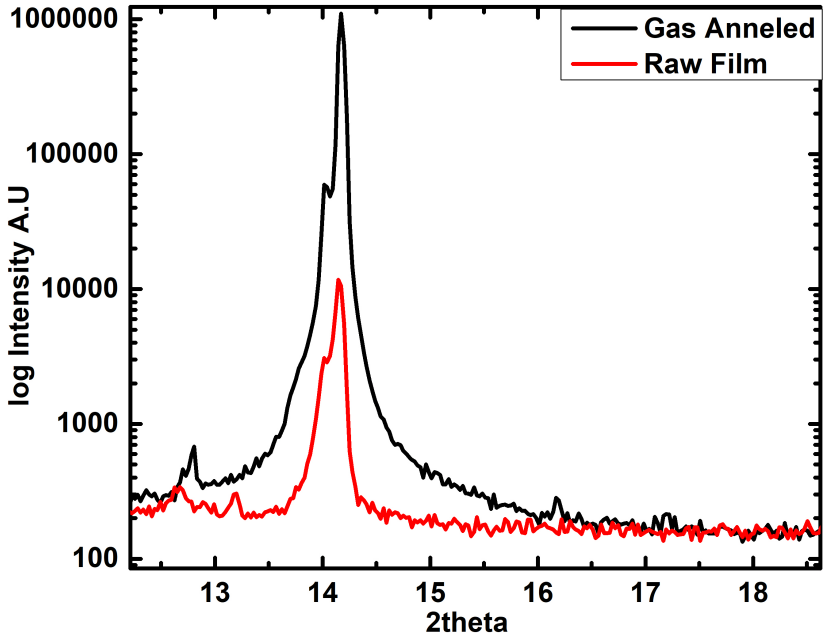

Figure 6.20: Logarithmic Intensity graph of (110) XRD peak of Gas annealed and raw film of $MAPbI_3$

Scanning Electron Microscopy

Scanning Electron Microscopy (SEM) is a potent visualization method employed to capture detailed, two-dimensional representations of a sample's surface. This technique delivers comprehensive insights about the sample's surface topography, structure, and composition on a micro- to nanoscale level. SEM proves crucial for the characterization of surface properties, structural integrity, and material composition.

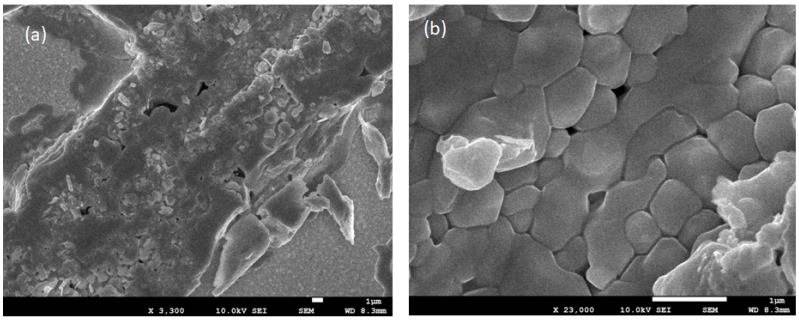

Figure 6.21: SEM images of $MAPbI_3$ raw film

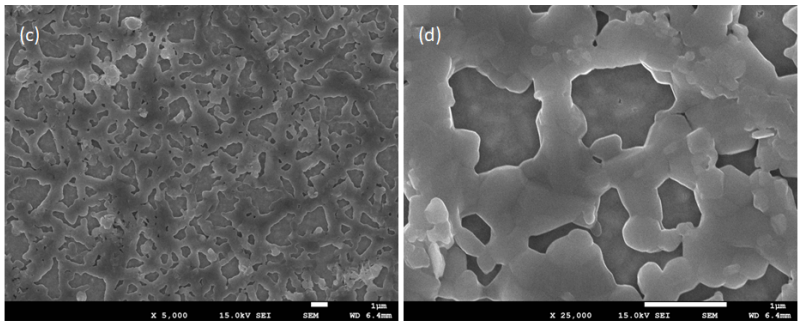

Figure 6.22: SEM images of $MAPbI_3$ Anti-solvent treated film

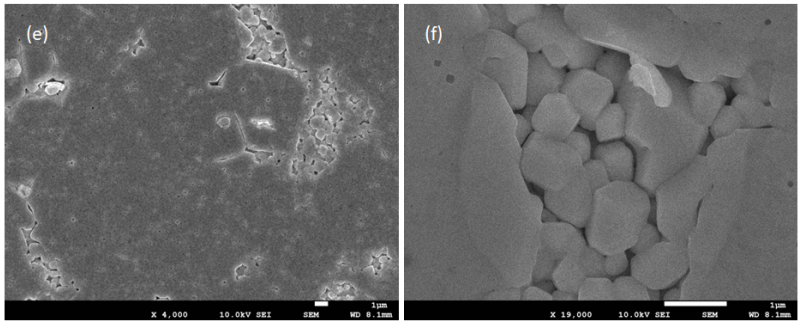

Figure 6.23: SEM images of $MAPbI_3$ gas healed film

We found that the spin-coated and annealed film (termed as raw film Fig. 6.21 (a) and (b)) had a non-uniform coverage on FTO and therefore, it left a lot of empty space between the grains. Such voids within the film are likely regions where the HTL or top conducting electrode can directly connect with the bottom leading to electrical shorting pathways. A similar sort of poor surface coverage was observed with the anit-solvent-coated $MAPbI_3$ film which is evident from Figure 6.21 (a). However, the gas-healed perovskite had good surface coverage with minimally exposed bottom FTO as evident from Figure 6.23 (e). The magnified view of Figure 6.23 (f) shows the healed perovskite film consisting of some large grains $\geqslant$ 400 – 500 nm agreeing well with the XRD data. Since the raw film and anti-solvent quenched films have predominantly large pinholes the devices were fabricated on gas-healed perovskite films. The surface of $MAPbI_3$ is quite rougher. The grains are quite small and visible for the case of raw $MAPbI_3$ but it gets bigger due to gas annealing as supported by the XRD data as well.

6.2.2 Fabricated PSCs results

The PSC architecture (FTO/SnO_2/$MAPbI_3$/Spiro/Au) was fabricated successfully according to the procure mentioned in experimental methods. After fabrication, these cells were tested under a solar simulator to check theirs. After fabrication, these cells were tested in a solar simulator to check their response when illuminated with light.

I-V measurement

I-V (current-voltage) measurements are a fundamental technique used to characterize the electrical performance of solar cells. These measurements provide valuable information about the device's power output, efficiency, and key parameters such as open-circuit voltage (Voc), short-circuit current (Isc), fill factor (FF), and maximum power point (MPP). It allows us to evaluate the electrical performance of perovskite solar cells, assess the impact of different device configurations or processing conditions, and compare the efficiency of various solar cell designs. These measurements help in optimizing device performance and understanding the underlying physics of the perovskite material.

Solar Simulator

A solar simulator is a device used in the testing and characterization of solar cells, including perovskite solar cells. It simulates the light conditions that the solar cell would experience under natural sunlight, allowing for accurate and controlled measurements of the device's electrical performance. The simulator was adjusted in such a way as to give AM1.5 spectra. The light intensity was adjusted to mimic the standard sunlight condition (1 sun) utilizing a fluxmeter. Utilizing a Keithley model 2450, the current-voltage behavior was captured under the source in a range from -0.8 to 1.2V, with a pause of 20 seconds implemented during each sweep.

Figure 6.24: Solar Simulator setup

A JV curve, alternatively referred to as the I-V curve or current-voltage curve, visually depicts the correlation between the current and voltage in a perovskite solar cell under diverse operational states. This graph offers significant insights into the device's electrical traits and operational efficiency. This curve is generated by varying the voltage and concurrently monitoring the resultant current. The examination of the JV curve enables the calculation of parameters like Voc, Jsc, FF, and the PCE of the device.

Fig.(6.25) shows the J-V characteristics of the fabricated PSCs. The photovltaic parameters exhibit open circuit voltage (V_{oc}) of 0.98V and short circuit current density (J_{sc}) of 23.75mA/cm^2. The fill factor (FF) calculated from eq.(4.15) comes out to be 28.14%. Similarly, Power Conversion Efficiency (PCE) calculated from eq.(4.17) is 6.5%. The J_{sc} and V_{oc} obtained are quite near to the literature value. While the FF is significantly low which might be due to the presence of defects with the perovskite or at the interface of perovskite-ETL or perovskite-HTL. Spiro-METAD which is used as HTL, is intrinsically a poor p-type semiconductor. Though we have put LiTFSI as a doping additive in the SpiroMeOTAD, it needs specialized dopants such as (FK209 Co(II) PF_6 Dyesol). Else, the ambient oxygen-induced doping could work, however, it is unreliable due to the presence of moisture in the air. Hence, we hypothesize that the insufficient oxidation

of Spiro-MeOTAD may contribute to a high series resistance within the device, resulting in a suboptimal fill factor. Additionally, the presence of cracks and pinholes within the film suggests an uptick in series resistance and a corresponding decline in shunt resistance.

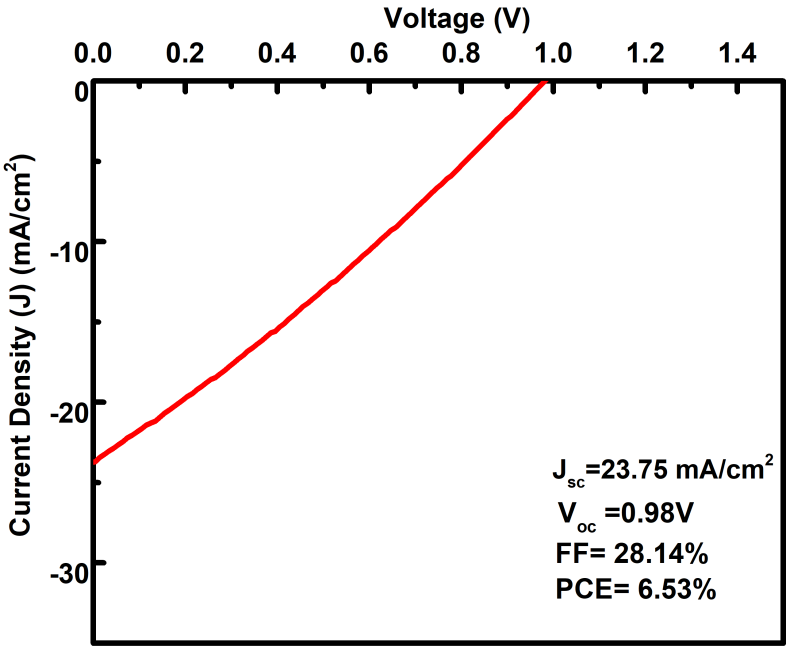

Fig 6.22 : J-V Curve

Figure 6.25: J-V curve of fabricated N-I-P architecture

6.3 Comparison of simulated and experimental results

In this section, the comparison of experimental and simulated data from the Transfer matrix model and the drift Diffusion model is done.

6.3.1 J-V curve comparison

In this section, we will be comparing our experimental J-V curve with the J-V curve from Drift Diffusion Modeling. In Fig (6.26) the blue curve is representing the ideal simulated J-V curve generated before doing the fabrication. The input parameters used for this simulation were taken from

the literature [54]. This has been generated by assuming series resistance of 4 Ω cm^2, shunt resistance of 1 × 10^5 Ω cm^2, the absorber band gap of 1.50 eV and capture cross section of electrons and holes to be 1 × 10^{-15}. The photovoltaic parameters of this simulated curve include Jsc= 27.48 mA/cm^2 ,Voc=1.11 V, FF= 71.31 % ,PCE= 22.50 %.

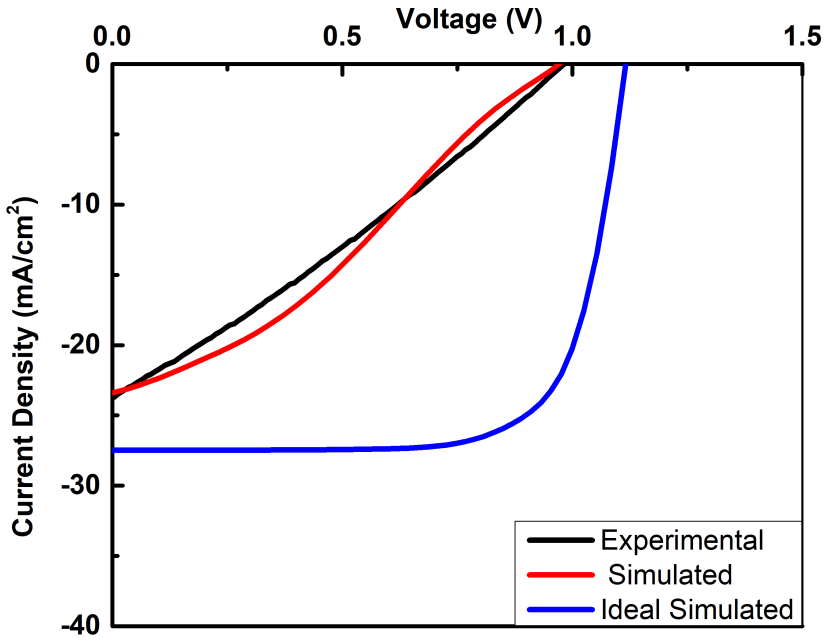

Figure 6.26: J-V curve of simulated (red), ideal (blue) and reverse simulated (black) N-I-P PSCs

The black one represents the experimental data in Fig (6.25). The red curve was the simulated data after analyzing the fabricated PSCs. It has been performed to understand the exact reason for achieving lesser photovoltaic parameters. This curve was achieved by increasing the capture cross-section of holes and electrons from 10^{-14} to 10^{-12} respectively indicating the increase in recombination loss. Increase in series resistance from 6 Ω cm^2 to 10 Ω cm^2, and shunt resistance from 1 × 10^5 to 1 × 10^3 Ω cm^2. Increase in defect density from 10^{15} to 10^{16} cm^{-3}.

Chapter 7

Conclusion and Future scope

"In summary, this thesis offers a deep dive into the simulation-driven approach used to uncover insights into light management and charge transport within the perovskite solar cell stack. A comprehensive analysis was conducted using both the Transfer Matrix Model (TMM) and the Drift-Diffusion Model (DDM), supplemented by experimental results, yielding several interesting findings.

1. To begin with, we demonstrated that the Python code based on the TMM is proficient in performing optical analysis of the multilayered perovskite solar cell (PSC) stack. This highlights its significance in discerning how light is captured in each layer and the source of optical losses therein. We fine-tuned the code to identify the External Quantum Efficiency (EQE) and consequently, the idealized Jsc for different architectures and materials. The Jsc derived from the TMM, DDM, and our experimental findings showed a satisfactory correlation for the device stack that we simulated.

2. However, the TMM simulation focused only on optical analysis, limiting its results to the simulated Jsc as the solitary photovoltaic parameter. To simulate Voc, FF, and subsequently PCE, we employed the SCAPS-1D simulation tool, based on the Drift-diffusion model, for the multilayered structure of PSCs. This tool broadened our theoretical comprehension of the photovoltaic parameter's dependency on factors such as thickness, defect density, the interfacial defect density of the layers of PSCs, and many more input parameters. Additionally, the software

proved useful in determining the reasons for not achieving desirable experimental results. Among the notable findings was the positive correlation between PCE and dopant density in the active perovskite layer beyond a specific doping density threshold. This finding suggests that by increasing the dopant carrier density to 10^{16} – 10^{17} cm^{-3}, thereby inducing p-type behavior in the perovskite layer, we could potentially enhance the PCE of n-i-p architecture from 23% to 28%.

3. Finally, we fabricated an n-i-p architecture PSC, eachieving Voc close to 1V, Jsc of 23.75 mA/cm2, a fill factor of 28%, and a PCE of 6.5%. While the Voc and Jsc closely matched the simulated results for an idealized device, the fill factor was disappointingly low. As such, we utilized drift-diffusion simulation to back-estimate and identify the source of this subpar performance. We theorize that the primary cause of this underperformance is poorly oxidized Spiro-METAD, resulting in high series resistance and low shunt resistance, as suggested by the simulated JV curve.We believe the path forward involves the application of innovative and controlled doping strategies for Spiro-MEOTAD.

All in all, this thesis has offered insights into the alignment between simulated and experimental outcomes. The findings emphasize the need to consider the broader significance or relevance for experimentalists. This research, it is hoped, will serve as a springboard for future studies, furthering advancements in perovskite solar cells. Moving forward, the TMM model can be integrated within the DDM framework to provide a comprehensive suite for optical and electrical analysis of PSCs."

References

[1] C. E. Fritts, "On the fritts selenium cells and batteries," *Journal of the Franklin Institute*, vol. 119, no. 3, pp. 221–232, 1885.

[2] D. M. Chapin, C. S. Fuller, and G. L. Pearson, "A new silicon p-n junction photocell for converting solar radiation into electrical power," *Journal of applied physics*, vol. 25, no. 5, pp. 676–677, 1954.

[3] M. A. Green, K. Emery, Y. Hishikawa, and W. Warta, "Solar cell efficiency tables (version 36)," *Progress in photovoltaics: research and applications*, vol. 18, no. 5, p. 346, 2010.

[4] A. Chirilă, S. Buecheler, F. Pianezzi, *et al.*, "Highly efficient cu (in, ga) se2 solar cells grown on flexible polymer films," *Nature materials*, vol. 10, no. 11, pp. 857–861, 2011.

[5] N. Romeo, A. Bosio, V. Canevari, and A. Podesta, "Recent progress on cdte/cds thin film solar cells," *Solar Energy*, vol. 77, no. 6, pp. 795–801, 2004.

[6] R. V. Angadi, B. Revanasiddesh, and P. Vineet Kumar, "A review on different types of materials employed in solar photovoltaic panel," *Int. J. Eng. Res. Technol*, vol. 7, no. 8, 2019.

[7] Q. A. Akkerman, V. D'Innocenzo, S. Accornero, *et al.*, "Tuning the optical properties of cesium lead halide perovskite nanocrystals by anion exchange reactions," *Journal of the American Chemical Society*, vol. 137, no. 32, pp. 10 276–10 281, 2015.

[8] G. E. Eperon, S. D. Stranks, C. Menelaou, M. B. Johnston, L. M. Herz, and H. J. Snaith, "Formamidinium lead trihalide: A broadly

tunable perovskite for efficient planar heterojunction solar cells," *Energy & Environmental Science*, vol. 7, no. 3, pp. 982–988, 2014.

[9] A. Kojima, K. Teshima, Y. Shirai, and T. Miyasaka, "Organometal halide perovskites as visible-light sensitizers for photovoltaic cells," *Journal of the american chemical society*, vol. 131, no. 17, pp. 6050–6051, 2009.

[10] J. Jeong, M. Kim, J. Seo, *et al.*, "Pseudo-halide anion engineering for α-fapbi3 perovskite solar cells," *Nature*, vol. 592, no. 7854, pp. 381–385, 2021.

[11] A. K. Jena, A. Kulkarni, and T. Miyasaka, "Halide perovskite photovoltaics: Background, status, and future prospects," *Chemical reviews*, vol. 119, no. 5, pp. 3036–3103, 2019.

[12] Y. Jiang, M. A. Green, R. Sheng, and A. Ho-Baillie, "Room temperature optical properties of organic–inorganic lead halide perovskites," *Solar Energy Materials and Solar Cells*, vol. 137, pp. 253–257, 2015.

[13] J.-S. Yeo, R. Kang, S. Lee, *et al.*, "Highly efficient and stable planar perovskite solar cells with reduced graphene oxide nanosheets as electrode interlayer," *Nano Energy*, vol. 12, pp. 96–104, 2015.

[14] P. Qin, S. Tanaka, S. Ito, *et al.*, "Inorganic hole conductor-based lead halide perovskite solar cells with 12.4% conversion efficiency," *Nature communications*, vol. 5, no. 1, p. 3834, 2014.

[15] Z. Ren, A. Ng, Q. Shen, *et al.*, "Thermal assisted oxygen annealing for high efficiency planar ch3nh3pbi3 perovskite solar cells," *Scientific Reports*, vol. 4, no. 1, pp. 1–6, 2014.

[16] T. Oku, "Crystal structures of perovskite halide compounds used for solar cells," *Reviews on Advanced Materials Science*, vol. 59, no. 1, pp. 264–305, 2020.

[17] V. M. Goldschmidt, "Die gesetze der krystallochemie," *Naturwissenschaften*, vol. 14, no. 21, pp. 477–485, 1926.

[18] Z. Li, M. Yang, J.-S. Park, S.-H. Wei, J. J. Berry, and K. Zhu, "Stabilizing perovskite structures by tuning tolerance factor: Formation of formamidinium and cesium lead iodide solid-state alloys," *Chemistry of Materials*, vol. 28, no. 1, pp. 284–292, 2016.

[19] G. Kieslich, S. Sun, and A. K. Cheetham, "An extended tolerance factor approach for organic–inorganic perovskites," *Chemical science*, vol. 6, no. 6, pp. 3430–3433, 2015.

[20] X. Zhou, J. Jankowska, H. Dong, and O. V. Prezhdo, "Recent theoretical progress in the development of perovskite photovoltaic materials," *Journal of energy chemistry*, vol. 27, no. 3, pp. 637–649, 2018.

[21] Z. Li, T. R. Klein, D. H. Kim, *et al.*, "Scalable fabrication of perovskite solar cells," *Nature Reviews Materials*, vol. 3, no. 4, pp. 1–20, 2018.

[22] L. M. Fraas and L. M. Fraas, "History of solar cell development," *Low-cost solar electric power*, pp. 1–12, 2014.

[23] M. Paulescu, E. Paulescu, P. Gravila, *et al.*, "Solar radiation measurements," *Weather Modeling and Forecasting of PV Systems Operation*, pp. 17–42, 2013.

[24] A. Pais, "Einstein and the quantum theory," *Reviews of modern physics*, vol. 51, no. 4, p. 863, 1979.

[25] H. Águas, T. Mateus, A. Vicente, *et al.*, "Thin film silicon photovoltaic cells on paper for flexible indoor applications," *Advanced Functional Materials*, vol. 25, no. 23, pp. 3592–3598, 2015.

[26] M. M. Lee, J. Teuscher, T. Miyasaka, T. N. Murakami, and H. J. Snaith, "Efficient hybrid solar cells based on meso-superstructured organometal halide perovskites," *Science*, vol. 338, no. 6107, pp. 643–647, 2012.

[27] H.-S. Kim, C.-R. Lee, J.-H. Im, *et al.*, "Lead iodide perovskite sensitized all-solid-state submicron thin film mesoscopic solar cell with efficiency exceeding 9%," *Scientific reports*, vol. 2, no. 1, p. 591, 2012.

[28] T. Leijtens, K. Bush, R. Cheacharoen, R. Beal, A. Bowring, and M. D. McGehee, "Towards enabling stable lead halide perovskite solar cells; interplay between structural, environmental, and thermal stability," *Journal of Materials Chemistry A*, vol. 5, no. 23, pp. 11 483–11 500, 2017.

[29] I. Mesquita, L. Andrade, and A. Mendes, "Effect of relative humidity during the preparation of perovskite solar cells: Performance and stability," *Solar Energy*, vol. 199, pp. 474–483, 2020.

[30] J. Idıgoras, F. J. Aparicio, L. Contreras-Bernal, *et al.*, "Enhancing moisture and water resistance in perovskite solar cells by encapsulation with ultrathin plasma polymers," *ACS Applied materials & interfaces*, vol. 10, no. 14, pp. 11 587–11 594, 2018.

[31] B. Brunetti, C. Cavallo, A. Ciccioli, G. Gigli, and A. Latini, "On the thermal and thermodynamic (in) stability of methylammonium lead halide perovskites," *Scientific reports*, vol. 6, no. 1, pp. 1–10, 2016.

[32] C. Eames, J. M. Frost, P. R. Barnes, B. C. O'regan, A. Walsh, and M. S. Islam, "Ionic transport in hybrid lead iodide perovskite solar cells," *Nature communications*, vol. 6, no. 1, p. 7497, 2015.

[33] Y. Kumar, E. Regalado-Perez, J. J. Jerónimo-Rendón, and X. Mathew, "Effect of cs+ and k+ incorporation on the charge carrier lifetime, device performance and stability in perovskite solar cells," *Solar Energy Materials and Solar Cells*, vol. 236, p. 111 512, 2022.

[34] T. Alerte, J. P. Edwards, C. M. Gabardo, *et al.*, "Downstream of the co2 electrolyzer: Assessing the energy intensity of product separation," *ACS Energy Letters*, vol. 6, no. 12, pp. 4405–4412, 2021.

[35] D. Zhang, D. Li, Y. Hu, A. Mei, and H. Han, "Degradation pathways in perovskite solar cells and how to meet international standards," *Communications Materials*, vol. 3, no. 1, p. 58, 2022.

[36] A. Abate, "Perovskite solar cells go lead free," *Joule*, vol. 1, no. 4, pp. 659–664, 2017.

[37] A. Taya, S. Kumar, T. A. Hackett, and M. K. Kashyap, "Optical absorption and stability enhancement in mixed lead, tin, and germanium hybrid halide perovskites for photovoltaic applications," *Vacuum*, vol. 201, p. 111 106, 2022.

[38] P. Wu and F. Zhang, "Recent advances in lead chemisorption for perovskite solar cells," *Transactions of Tianjin University*, vol. 28, no. 5, pp. 341–357, 2022.

[39] O. V. Mikhnenko, M. Kuik, J. Lin, N. van der Kaap, T.-Q. Nguyen, and P. W. Blom, "Trap-limited exciton diffusion in organic semiconductors," *Advanced Materials*, vol. 26, no. 12, pp. 1912–1917, 2014.

[40] G. Wetzelaer, M. Kuik, H. Nicolai, and P. Blom, "Trap-assisted and langevin-type recombination in organic light-emitting diodes," *Physical Review B*, vol. 83, no. 16, p. 165 204, 2011.

[41] Z. Li, T. Klein, D. Kim, M. Yang, J. Berry, and K. Zhu, "Scaling up perovskite photovoltaics: Progress, challenges, and outlook of a transformational technology," *Nat. Rev. Mater*, vol. 3, p. 18 017, 2018.

[42] V. More, V. Shivade, and P. Bhargava, "Effect of cleaning process of substrate on the efficiency of the dssc," *Transactions of the Indian Ceramic Society*, vol. 75, no. 1, pp. 59–62, 2016.

[43] F. Yang, M. A. Kamarudin, P. Zhang, G. Kapil, T. Ma, and S. Hayase, "Enhanced crystallization by methanol additive in antisolvent for achieving high-quality mapbi3 perovskite films in humid atmosphere," *ChemSusChem*, vol. 11, no. 14, pp. 2348–2357, 2018.

[44] Z. Li, X. Wang, Z. Wang, *et al.*, "Ammonia for post-healing of formamidinium based perovskite films," *Nature Communications*, vol. 13, no. 1, p. 4417, 2022.

[45] Y. Wei, W. Li, S. Xiang, *et al.*, "Precursor effects on methylamine gas-induced ch3nh3pbi3 films for stable carbon-based perovskite solar cells," *Solar Energy*, vol. 174, pp. 139–148, 2018.

[46] Z. Zhou, Z. Wang, Y. Zhou, *et al.*, "Methylamine-gas-induced defect-healing behavior of ch3nh3pbi3 thin films for perovskite solar cells," *Angewandte Chemie*, vol. 127, no. 33, pp. 9841–9845, 2015.

[47] E. R. Schütz, A. Fakharuddin, Y. Yalcinkaya, *et al.*, "Reduced defect density in crystalline halide perovskite films via methylamine treatment for the application in photodetectors," *APL Materials*, vol. 10, no. 8, p. 081 110, 2022.

[48] S. Wu and H.-J. Butt, "Near-infrared photochemistry at interfaces based on upconverting nanoparticles," *Physical Chemistry Chemical Physics*, vol. 19, no. 35, pp. 23 585–23 596, 2017.

[49] T. Thornber, O. S. Game, E. J. Cassella, *et al.*, "Nonplanar spray-coated perovskite solar cells," *ACS Applied Materials & Interfaces*, vol. 14, no. 33, pp. 37 587–37 594, 2022.

[50] T. M. Brenner, D. A. Egger, L. Kronik, G. Hodes, and D. Cahen, "Hybrid organic—inorganic perovskites: Low-cost semiconductors with intriguing charge-transport properties," *Nature Reviews Materials*, vol. 1, no. 1, pp. 1–16, 2016.

[51] J. Euvrard, O. Gunawan, and D. B. Mitzi, "Impact of pbi2 passivation and grain size engineering in ch3nh3pbi3 solar absorbers as revealed by carrier-resolved photo-hall technique," *Advanced Energy Materials*, vol. 9, no. 47, p. 1 902 706, 2019.

[52] A. Zohar, I. Levine, S. Gupta, *et al.*, "What is the mechanism of mapbi3 p-doping by i2? insights from optoelectronic properties," *ACS Energy Letters*, vol. 2, no. 10, pp. 2408–2414, 2017.

[53] I. Levine, S. Gupta, T. M. Brenner, *et al.*, "Mobility–lifetime products in mapbi3 films," *The journal of physical chemistry letters*, vol. 7, no. 24, pp. 5219–5226, 2016.

[54] Y. Raoui, H. Ez-Zahraouy, N. Tahiri, O. El Bounagui, S. Ahmad, and S. Kazim, "Performance analysis of mapbi3 based perovskite solar cells employing diverse charge selective contacts: Simulation study," *Solar Energy*, vol. 193, pp. 948–955, 2019.